# High magnetic anisotropy and magnetocaloric effects in single crystal Cr<sub>2</sub>Te<sub>3</sub>

Anirban Goswami<sup>1</sup>, Nicholas Ng<sup>2,3</sup>, AM Milinda Abeykoon<sup>4</sup>, Emmanuel Yakubu<sup>1</sup> and Samaresh Guchhait<sup>1\*</sup>

- 1. Department of Physics and Astronomy, Howard University, Washington, DC 20059, USA
- 2. Department of Chemistry, The Johns Hopkins University, Baltimore, MD 21218, USA
- 3. Institute for Quantum Matter, The William H. Miller III Department of Physics and Astronomy, The Johns Hopkins University, Baltimore, MD 21218, USA
- 4. National Synchrotron Light Source-II, Brookhaven National Laboratory, Upton, NY 11733, USA

#### **Abstract**

We report a systematic investigation of anisotropic magnetocaloric effects in single crystal  $Cr_2Te_3$ . Single crystal samples are synthesized by chemical vapor transport and characterized by X-ray and Laue diffraction methods. The maximum magnetic entropy change  $-\Delta S_M^{max}$  is 4.50 J kg<sup>-1</sup> K<sup>-1</sup> for the easy *c*-axis (3.36 J kg<sup>-1</sup> K<sup>-1</sup> for the hard axis along *ab*-plane) and the relative cooling power RCP is 296.7 J kg<sup>-1</sup> for the easy *c*-axis (183.84 J kg<sup>-1</sup> for the hard axis along *ab*-plane) for a magnetic field change of 9 T near the Curie temperature. The magneto-crystalline anisotropy constant  $K_u$  is estimated to be 580.12 kJ m<sup>-3</sup> at 140 K, decreasing to 148.60 kJ m<sup>-3</sup> at 168 K. Meanwhile, the maximum of the rotational magnetic entropy change  $-\Delta S_M^R(T, H)$  between the *c*-axis and the *ab*-plane is about 1.14 J kg<sup>-1</sup> K<sup>-1</sup> for magnetic-field change of 9 T. The critical exponents are estimated by analyzing magnetocaloric effects, which indicate 2D-Ising type magnetic system. The accuracy of estimated critical exponents is verified by scaling analysis. The maximum magnetic entropy change  $-\Delta S_M^{max} \sim 5.25$  J kg<sup>-1</sup> K<sup>-1</sup> (along the *c*-axis) and the corresponding adiabatic temperature change  $\Delta T_{ad} \sim 3.31$  K (along the *c*-axis) are estimated by analyzing heat capacity measurements with a magnetic field up to 9 T.

#### Introduction

After the important breakthrough of long-range intrinsic magnetism down to the monolayer limit in two-dimensional materials, transition-metal chalcogenides have received renewed interest from

<sup>\*</sup>Email address of correspondence: samaresh.guchhait@Howard.edu

the academic community because a few of these binary phases may describe room temperature ferromagnetism down to monolayer limit which could be suitable for low dimensional spintronics applications <sup>1</sup>. The remarkable potential of device applications lies in the tunable correlation between the structure and physical properties of ultrathin layers of transition metal chalcogenides.<sup>2–7</sup>. Among these transition metal chalcogenides, chromium telluride (Cr<sub>x</sub>Te<sub>y</sub>) binary phases have gained significant attention because of their potential applications in spintronics. Previously, many binary phases of Cr<sub>x</sub>Te<sub>y</sub> (such as, CrTe<sup>8</sup>, CrTe<sup>9,10</sup>, Cr<sub>2</sub>Te<sup>11-14</sup>, Cr<sub>3</sub>Te<sub>4</sub><sup>15</sup>, Cr<sub>5</sub>Te<sub>6</sub><sup>16</sup>, Cr<sub>0.62</sub>Te <sup>17</sup>, Cr<sub>5</sub>Te<sub>8</sub><sup>18,19</sup>) have been studied to explore their structure-property relationships. Some Cr-Te binary phases exhibit near room temperature ferromagnetic properties inbulk and layered forms<sup>8,15,16,20</sup>. Reportedly, these compounds exhibit ferromagnetic properties, with Curie temperatures (TC) ranging from 160 to 340 K, depending on their chromium concentration<sup>21</sup>. In these compounds, the c-axis features alternating stacks of chromium-deficient and chromium-rich layers. The vacancy within the chromium content significantly influences both their structure and magnetic properties.<sup>22</sup>. Recently, there has been a report of critical behavior and magnetocaloric effect in Se-doped CrTe where a very high relative cooling power (RCP) and a large change of magnetic entropy are observed<sup>23</sup>. There is also another report of the evolution of this NiAS-type structure with Se content<sup>24</sup>.

In this article, anisotropic magnetocaloric properties of single crystal Cr<sub>2</sub>Te<sub>3</sub> are reported. The magnetic properties of bulk Cr<sub>2</sub>Te<sub>3</sub> and the correlation between their structural and magnetic properties have been reported before<sup>25–28</sup>. Recently, there have been more studies on Cr<sub>2</sub>Te<sub>3</sub> in both bulk and layered forms<sup>11–14</sup>. The neutron diffraction study depicts ferromagnetic ordering of Cr moments in Cr<sub>2</sub>Te<sub>3</sub> along the *c*-axis and the volume of the unit cell decreases as the temperature decreases <sup>27,29</sup>. The average calculated magnetic moment is 2.7 μ<sub>B</sub>/Cr atom in this material, which is significantly smaller than that of an isolated Cr<sup>3+</sup> ion<sup>30</sup>. According to John Goodenough<sup>31</sup>, this reduction of the effective magnetic moment may originate from a spiral antiferromagnetic spin structure. However, a different approach suggested by A. F. Anderson *et al.*<sup>30</sup> indicates that this phenomenon may be due to magnetic moment canting. Yao Wen *et al.* reported that the Curie temperature of Cr<sub>2</sub>Te<sub>3</sub> can be tuned close to room temperature (~280 K) by decreasing sample thickness to 1 or 2 unit-cell limits, which is also supported by the anomalous Hall effect measurement<sup>14</sup>. Fang Wang *et al.* reported the organic solution phase synthesis of Cr<sub>2</sub>Te<sub>3</sub> nanorods with ultra-high coercivity<sup>11</sup>. Roy *et al.* have grown Cr<sub>2</sub>Te<sub>3</sub> thin films by molecular beam epitaxy which show large perpendicular magnetic anisotropy<sup>12,13</sup>.

However, our goal here is to explore the anisotropic magnetocaloric properties of single crystal Cr<sub>2</sub>Te<sub>3</sub> which has not been reported before. Magnetic refrigeration using the magnetocaloric effect (MCE) has a huge potential to meet the worldwide demand for environmentally friendly, and energy-efficient thermal management<sup>32,33</sup>. As Cr<sub>2</sub>Te<sub>3</sub> exhibits a second-order magnetic phase transition, it exhibits a change in magnetic entropy over a broad temperature range, and it does not exhibit any magnetic or thermal hysteresis. Due to the 2<sup>nd</sup> order nature of its magnetic phase transition, this material may be suitable for potential magnetocaloric applications because there is a gradual transition from the low-temperature phase to the high-temperature phase.

In contrast, in a 1<sup>st</sup> order magnetic phase transition there is a temperature range where both phases coexist<sup>34</sup>. Till date, anisotropic magnetocaloric properties have been reported in other layered

magnetic materials, such as  $CrI_3^{35}$ ,  $CrCI_3^{36,37}$ ,  $CrSbSe_3^{38}$ , and  $Cr_4Te_5^{20}$ . There are reports on estimating critical exponents by analyzing the anisotropic magnetocaloric effects in some materials, such as  $Cr_2Ge_2Te_6^{39}$  and  $Cr_5Te_8^{19}$ .

Here, we report the anisotropic magnetocaloric properties of a single crystal Cr<sub>2</sub>Te<sub>3</sub> sample by studying field-dependent isothermal magnetization along its *c*-axis and *ab*-plane. By analyzing the magnetocaloric effects (MCE), we show there is a 2<sup>nd</sup> order (paramagnetic to ferromagnetic) magnetic phase transition. Moreover, by estimating its magnetocaloric effects as a function of field and temperature, we calculate its full width at half maximum (FWHM), and refrigerant capacity or relative cooling power (RCP). With the help of these physical parameters, the critical exponents related to its magnetic phase transition are estimated. We then verify the accuracy of our estimated critical exponents by scaling analysis. Finally, we estimate adiabatic temperature change and change of magnetic entropy from the temperature and field dependent heat capacity measurements.

#### Sample Synthesis and Phase Characterizations

Single crystal samples are synthesized by the chemical vapor transport (CVT) method. These CVT experiments are performed in a Thermo Scientific Lindberg Blue M three-zone furnace equipped with UP150 model program controllers. Cr (Alfa Aesar, powder, -100+325 mesh, 99.99% metals basis) and Te (Thermo Scientific, shot, 2-5 mm diameter, 99.9999% metals basis) are used as received without further purification. Stoichiometric amounts of Cr and Te are combined in a fused quartz tube. Between 35-50 mg of solid iodine is used as the vapor transport agent. The iodine is added to the tube, which is then sealed under vacuum. The sealed tube is, at minimum, long enough to equal the distance between two zones of a three-zone furnace. This tube is then placed inside the three-zone furnace. All three zones are heated up at a rate of 100°C per hour, with the charge zone reaching 900°C and the crystallization zone reaching 800°C. This temperature gradient is held for one week, then the furnace is cooled at a rate of 100°C per hour to room temperature.

Room temperature powder x-ray diffraction (XRD) measurements were conducted at the Pair Distribution Function (PDF) beamline (28-ID-1) of the National Synchrotron Light Source-II. We collected our data on grounded single crystal samples in capillary transmission geometry using a PerkinElmer amorphous silicon detector placed 1000 mm downstream from the sample <sup>17</sup>. The setup utilized a 74.5 keV ( $\lambda = 0.1665$  Å) x-ray beam. Two-dimensional diffraction images were radially integrated to obtain intensity vs. 2-theta data using the pyFAI software package. The Rietveld refinement was conducted by utilizing the GSAS-II software package<sup>40</sup>. Figure 1 (a) shows the Rietveld fit to experimental data using the symmetry space group P31c, which agrees well with previous crystallographic studies on this material<sup>27,41</sup>. This is a different space group from the reported Cr<sub>0.62</sub>Te phase symmetry space group P3m1 which is also the same as the reported symmetry space group of  $Cr_5Te_8$  phase <sup>17,42</sup>. The refined unit cell parameters are a, b =6.7920(2) Å, and c = 12.0887(2) Å. The refined fractional coordinates, occupancies of Cr and Te sites, and the isotropic thermal displacement parameters (Uiso) are shown in the Supporting Information (Table S1). All Rietveld refinement fit parameters are also included in the Supporting Information (Table S2). Figure 1 (b) and (c) shows the refined crystal structure of trigonal Cr<sub>1.77</sub>Te<sub>3</sub> generated using the Vesta software package<sup>43</sup>. The Cr deficient site, 2c (0.3333, 0.6667, 0.2500) is shown with half-white half-purple balls. We believe that the Cr deficient sites are not correlated, rather they are randomly distributed throughout the lattice giving rise to short-range order. The

Laue diffraction is used to determine the crystallographic axes of the single crystal sample using structural parameters determined from the Rietveld refinement, which is shown in Figure 1(d). A good agreement between experimental and simulated Laue data indicates accuracy of our estimated crystal structure and phase by Rietveld refinement. The refined structural model well-agrees with literature confirming the synthesis of the correct compound.

#### **Results and discussions**

Figure 2 shows temperature (T) dependent magnetization (M) along the *c*-axis and parallel to the *ab*-plane (out-of-plane and in-plane, respectively) for a single crystal sample with an application of 0.1 T magnetic field (H). These M(T) curves demonstrate an anisotropic magnetic response when fields are applied along two distinct directions for temperatures below the transition temperature. M(T) for field parallel to the *ab*-plane is shown in the inset of Figure 2 for clarity. Along the *c*-axis, a rapid upturn occurs around 170 K upon cooling, signifying a paramagnetic to ferromagnetic phase transition. The magnetization along the *c*-axis is about 13 times greater than that along the *ab*-plane. The M(T) measurements point to a large uniaxial magnetic anisotropy in Cr<sub>2</sub>Te<sub>3</sub>. The difference between zero-field-cooling (ZFC) and field-cooling (FC) data below ~30 K is due to random orientation of finite-size magnetic domains<sup>44</sup>. A decrease of magnetization for magnetic field parallel to the *ab*-plane below the transition temperature in Fig. 2 is reported before for CrSiTe<sub>3</sub><sup>45</sup>, Cr<sub>1</sub><sup>36</sup>, Cr<sub>5</sub>Te<sub>8</sub><sup>47,48</sup>, etc. and explained as an effect of increasing magnetic anisotropy with decreasing temperature<sup>46</sup>. Temperature dependence of magnetic anisotropy of Cr<sub>2</sub>Te<sub>3</sub> is discussed below.

To confirm the nature of the paramagnetic-to-ferromagnetic phase transition, we have calculated the dM/dT vs T which is shown in Figure 3(a). This dM/dT vs T graphs show negative peaks for the field along both directions which give us an approximate phase transition temperature ~170 K, and this is in good agreement with the previously reported transition temperature of  $Cr_2Te_3$  sample<sup>49</sup>. The temperature-dependent inverse magnetic susceptibility curves are shown in Figure 3(b). The quasilinear portion in the paramagnetic phase has intercepts in the positive *x*-axis for the field along both directions (along the *c*-axis and parallel to the *ab*-plane) which indicates a paramagnetic-to-ferromagnetic phase transition. To calculate the Curie-Weiss temperature, the linear portions of the paramagnetic region of both curves are fitted with the equation  $1/\chi = (T-\theta)/C$ . From these fits, we get the Curie-Weiss temperature  $\theta_C = +194.290 \pm 2.333$  K and  $+183.138 \pm 0.634$  K along the *c*-axis and parallel to the *ab*-plane, respectively. These are consistent with previous studies of  $Cr_2Te_3$  which have shown ferromagnetic ordering down to the monolayer limit<sup>49</sup> and are also confirmed by the neutron diffraction studies<sup>30</sup>.

To further explore the field-dependent magnetization along the easy and hard axis, we performed isothermal field-dependent magnetization at 2 K, as shown in Figure 4. The M(H) at 2 K along the c-axis saturates at  $\sim 0.35$  T field but does not saturate along the ab-plane even at 9 T field. The saturated magnetic moment at 2 K for the H  $\parallel c$ -axis is 2.25  $\mu_B$ /Cr. The measured (unsaturated) magnetic moment at 2 K for H  $\parallel ab$ -plane is 2.14  $\mu_B$ /Cr at 9 T field. These results (Figures 2 and 4) confirm that the c-axis exhibits the magnetic easy axis of the single-crystal  $Cr_2Te_3$  sample.

To further explore magnetic anisotropy properties, we performed field-dependent isothermal magnetization studies around its phase transition temperature (~170 K). Figures 5(a) and 5(b) describe isothermal magnetizations from 140 to 210 K at 2 K interval for fields up to 9 T applied along the c-axis and parallel the ab-plane, respectively. All magnetic and heat capacity studies are performed using a Quantum Design Physical Property Measurement System (PPMS) 9 Tesla Dynacool model. There is a clear difference between field-dependent magnetization curves along the c-axis and ab-plane, particularly in the low-magnetic-field region. Below  $T_C$ , the magnetization along the c-axis tends to saturate for small fields, whereas it increases slowly with applied magnetic field along the ab-plane. This points to the presence of large magnetic anisotropy in Cr<sub>2</sub>Te<sub>3</sub>. The micromagnetic energy density can be expressed as  $E_A = K_u \sin^2(\theta - \phi)^{50}$ , where  $K_u$  is the uniaxial magneto-crystalline parameter,  $\theta$  is the orientation of the preferred magnetization,  $\phi$  is the orientation toward which the magnetization point. When  $\theta - \phi = 90^{\circ}$  (i.e., H || ab-plane), the magneto-crystalline anisotropy is maximum. The uniaxial anisotropy parameter Ku is related to the saturation field  $H_S$  and saturation magnetization  $M_S$  by  $2K_u/M_S = \mu_0 H_S$ , where  $\mu_0$  is the vacuum permeability. We estimate  $M_S$  by using a linear fit of M(H) curves for field parallel to the ab-plane above 6 T. The saturation magnetization monotonically decreases with increasing temperature. We then determined H<sub>S</sub> from the intersection point of two linear fits to isothermal M(H) curves for H || ab-plane: One corresponds to fitting the saturated regime at a high field, while the other corresponds to fitting the unsaturated linear regime at the low magnetic field. This procedure is explained in detail in the anisotropic magnetic entropy change studies of VI<sub>3</sub><sup>51</sup> and CrSbSe<sub>3</sub><sup>38</sup>. Figure 6 shows the temperature-dependent magnetic anisotropy, along with the temperaturedependent saturation magnetization and saturation magnetic field in the Figure 6 insets. The estimated  $K_u$  decreases monotonically from 580.1196 kJ m<sup>-3</sup> at 140 K to 150.6002 kJ m<sup>-3</sup> near  $T_C$ . The observed decrease in  $K_{\rm u}$ with temperature arises exclusively from local spin clusters fluctuating randomly around the macroscopic magnetization vector, activated by nonzero thermal energy 52,53. This rapid increase of magnetic anisotropy with decreasing temperature could explain the decrease of magnetization for H  $\parallel ab$ -plane with decreasing temperature below the phase transition, <sup>46</sup> as seen in Figure 2. To study anisotropic MCE in the single-crystal Cr<sub>2</sub>Te<sub>3</sub> system, we estimate changes in magnetic entropy along different axes in this material. The change of magnetic entropy -ΔS<sub>M</sub> (T, H) is defined as the following<sup>33,54</sup>:

$$\Delta S_M(T, H) = \int_0^H \left[ \frac{\partial S(T, H)}{\partial H} \right] dH$$
 (1a)

Using the Maxwell's relation  $\partial S(T, H)/\partial H = \partial M(T, H)/\partial T$ , this can be expressed as following:

$$\Delta S_M(T, H) = \int_0^H \left[ \frac{\partial M(T, H)}{\partial T} \right] dH$$
 (1b)

For isothermal magnetization measured at small discrete magnetic fields and temperature intervals,  $-\Delta S_M(T, H)$  is the isothermal change of entropy in the interval of the magnetic field from 0 to H and can be approximated as

$$\Delta S_M(T, H) = \frac{\int_0^H M(T_{i+1}, H) - \int_0^H M(T_{i}, H)}{T_{i+1} - T_i}$$
 (2)

The calculated  $-\Delta S_M$  values as a function of temperature in various fields up to 9 T applied along the c-axis and parallel to the ab-plane are shown in Figures 7(a) and 7(b), respectively. All these  $-\Delta S_M(T, H)$  curves show a pronounced peak around the phase transition temperature, and the peak asymmetrically broadens on both sides with increasing magnetic field. However, it is clear from these two figures that the  $-\Delta S_M$  curves along the ab-plane are much more asymmetric in comparison to  $-\Delta S_M$  curves along the c-axis. Also,  $-\Delta S_M$  reaches a maximum of  $\sim$ 4.5 J kg<sup>-1</sup> K<sup>-1</sup> along the c-axis and  $\sim$ 3.36 J kg<sup>-1</sup> K<sup>-1</sup> along the ab-plane. The small negative value of magnetic entropy change is observed in the case of H  $\parallel$  ab-plane at low magnetic field values below transition temperature. However, all the values are positive along the c-axis. This kind of behavior is reported before in CrI<sub>3</sub>  $^{35}$  and VI<sub>3</sub>  $^{51}$  and explained as an effect of the competition between the temperature dependence of magnetization and magnetic anisotropy. In Cr<sub>2</sub>Te<sub>3</sub>, magnetic anisotropy increases as temperature decreases (Figure 6), while magnetization for H  $\parallel$  ab-plane exhibits the opposite trend below the transition temperature (Figure 2). The rotational magnetic entropy change,  $\Delta S_M^R$  determined by rotating the field from the c-axis to the ab-plane can be expressed as:

$$\Delta S^{R}_{M} = S_{M}(T, H_{c}) - S_{M}(T, H_{ab}) = \Delta S_{M}(T, H_{c}) - \Delta S_{M}(T, H_{ab})$$
(3)

Figure 7(c) shows temperature-dependent rotational magnetic entropy change for different fields. The anisotropy is gradually suppressed at higher fields, as seen in Figure 7(c). Interestingly, it splits into many peaks (in the scattered pattern) on both sides of the T<sub>C</sub> for a field above 3 T for single-crystal Cr<sub>2</sub>Te<sub>3</sub>. Up to 3 T magnetic field, there is a visible peak near T<sub>C</sub>. But above 3 T, there is a discrepancy in the pattern of the curves, which is an indication of decreasing anisotropy due to the increasing magnetic field.

To further explore the nature of this magnetic phase transition, we use a proposed universal scaling analysis to analyze our - $\Delta S_M$  data. We first normalize all - $\Delta S_M$  curves against the respective maximum - $\Delta S_M^{max}$  value, namely,  $\Delta S_M/\Delta S_M^{max}$ . We then rescale the temperature T below and above  $T_C$ , as defined in the following equations:

$$\theta_{-} = (T_{peak} - T)/(T_{r1} - T_{peak}), \text{ for } T < T_{peak},$$
 (4)

$$\theta_{+} = (T - T_{peak})/(T_{r2} - T_{peak}), \text{ for } T > T_{peak},$$
 (5)

where  $\theta_{\pm}$  are the rescaled temperatures,  $T_{r1}$  and  $T_{r2}$  are temperatures of two selected reference points corresponding to  $-\Delta S_M(T_{r1}, T_{r2}) = -\Delta S_M^{max}/2$ . As shown in Figures 8(a)-(b), all  $-\Delta S_M(T, H)$  curves for different fields collapse into a single curve, implying a second-order magnetic phase transition in single-crystal  $Cr_2Te_3$ . In Figure 8(b), some  $-\Delta S_M(T, H)$  curves do not collapse into the scaled curve for a narrow window of the scaled temperature because of the highly asymmetric nature of these curves in this region. This type of phenomenon has been reported before for VI<sub>3</sub> <sup>56</sup>.

For a material undergoing a second-order magnetic phase transition<sup>57</sup>, the various parameters of  $\Delta S_M(T)$  curves obey different field-dependent power laws, as following<sup>58,59</sup>:

$$|\Delta S_{M}^{max}| = a H^{n}, \qquad (6)$$

$$\delta T_{\text{FWHM}} = m H^b,$$
 (7)

$$RCP = d H^{c}, (8)$$

Here  $\Delta S_M^{max}$  is the maximum value of  $-\Delta S_M$ ,  $\delta T_{FWHM}$  is the full width at half maximum of  $-\Delta S_M$  (T, H) curve and RCP is the relative cooling power. The RCP determines the cooling efficiency of a refrigerant and corresponds to the quantity of heat that can be transferred between the cold and hot sections of the refrigerator in an ideal thermodynamic system <sup>32,55</sup>. This process plays a vital role in magnetic refrigerators. RCP is expressed as:

$$RCP = \Delta S_{M}^{max} \times \delta T_{FWHM}$$
 (9)

Therefore,  $|\Delta S_M^{max}|$ , RCP, and  $\delta T_{FWHM}$  are all related to the applied magnetic field with power law relation, as expressed in equations (6)-(8). Here exponents c, n, and b are related to the critical exponents  $\beta$ ,  $\gamma$ , and  $\delta$ , by the following relations<sup>55</sup>:

$$c = 1 + 1/\delta, \tag{10a}$$

$$b = 1/\Delta = 1/\beta \delta, \tag{10b}$$

$$n(T_C) = 1 + \left[\frac{\beta - 1}{\beta + \gamma}\right] = 1 + \frac{1}{\delta} \left(1 - \frac{1}{\beta}\right).$$
 (10c)

Here,  $\beta$ ,  $\gamma$ , and  $\delta$  are called critical exponents of a magnetic phase transition<sup>60</sup>. Therefore, by analyzing the magnetocaloric effect (MCE) we will be able to estimate these critical exponents. The critical exponents obtained from the MCE analysis are reliable because it is a direct method <sup>61,62</sup>. These critical exponents are also related by the Widom's law:  $\delta = 1 + \gamma/\beta^{63}$ . Figures 9(a) and 9(b) represent the field dependence of  $-\Delta S_{\rm M}^{\rm max}$  and RCP for the field along the *c*-axis and parallel to the *ab*-plane, respectively. The calculated values of RCP are approximately 296.958 and 183.889 J kg<sup>-1</sup> field along the *c*-axis and parallel to the *ab*-plane, respectively, with a magnetic field change of 9 T. Fitting of  $-\Delta S_{\rm M}^{\rm max}$  gives  $n(T_{\rm C}) = 0.651 \pm 0.009$  and  $1.029 \pm 0.032$  for H || *c*-axis and H || *ab*-plane, respectively [Figures 9(a)-(b)]. Among these values, the *n* value along the *c*-axis is very close to 0.667 which is the mean-field model ( $\beta = 0.5$ ,  $\gamma = 1$ ) *n* value. Fittings of the RCP data give us  $c = 1.125 \pm 0.011$  and  $1.589 \pm 0.017$  [Figures 9(a)-(b)], which then yield  $\delta = 7.994$  and 1.699 for H || *c*-axis and H || *ab*-plane, respectively.

Similarly, Figures 10(a)-(b) show the magnetic field dependent  $\delta T_{\rm FWHM}$  for field applied along the c-axis and parallel to the ab-plane, respectively. The estimated values of  $\delta T_{\rm FWHM}$  are 65.914 K and 54.682 K for a magnetic field change of 9 T field along the c-axis and parallel to the ab-plane, respectively. These field dependent  $\delta T_{\rm FWHM}$  curves fit well with equation (7) and fittings of the  $\delta T_{\rm FWHM}$  curves give  $b = 0.529 \pm 0.005$  and  $0.648 \pm 0.004$  field along the c-axis and parallel to the ab-plane, respectively [Figures 10(a)-(b)]. Then using equation (10b) we estimate  $\Delta = 1.889$  and 1.544 field along the c-axis and parallel to the ab-plane respectively. After solving all these equations, we estimate  $\beta = 0.236$ ,  $\gamma = 1.652$ , and  $\delta = 7.994$  for H || c-axis whereas we estimate  $\beta = 0.909$ ,  $\gamma = 0.635$ , and  $\delta = 1.699$  for H || ab-plane. The estimated critical exponent values for fields applied along the ab-plane are different from those estimated values for field along the c-axis. We will

later verify their reliability by universal scaling analysis. Similar differences in estimated critical exponent values for two axes have been reported before for VI<sub>3</sub><sup>56</sup>. Table I shows our estimated critical exponent values with other reported and numerically estimated critical exponent values.

For a material undergoing a second-order magnetic phase transition, the maximum magnetic entropy change follows a power law dependence with applied magnetic field:  $-\Delta S^{max}_{M} = a H^{n}$ , where a is a constant and the exponent n is associated with the magnetic order. This can be expressed in another way  $n(T, H) = d \ln|\Delta S_{M}|/d \ln(H)$ . Using this expression, all n(T) curves for each magnetic field can be estimated. Figure 11 describes the n(T) for various fields. All n(T) curves follow a pattern described next. At low temperatures, well below  $T_{C}$ , n(T) is about 1. On the other side, well above  $T_{C}$ , n is close to 2 because of the Curie-Weiss law. At  $T = T_{C}$ , n(T) has a minimum. It could be found that with a field change of 9 T the n values are 1.09 and 1.81 far below and above  $T_{C}$ , respectively. This behavior perfectly aligns with the universal law of  $n^{59}$ . With a reduction of magnetic field, the n value remains nearly unchanged at and above the transition temperature. However, it deviates at a lower temperature which might be due to the magnetic anisotropy effect<sup>35</sup>.

For a second-order magnetic phase transition,  $-\Delta S_M$  vs. T corresponding to different magnetic fields can be rescaled using the scaled equation of state:  $H/M^{\delta} = f(\varepsilon/M^{1/\beta})$ , where  $\delta$  and  $\beta$  are critical exponents<sup>34,64</sup>. Here the reduced temperature  $\varepsilon = (T - T_C)/T_C$ ). The  $-\Delta S_M(T, H)$  can be rewritten in another form:

$$\Delta S_M(T, H) = H^{\frac{1-\alpha}{\Delta}} g\left(\frac{\varepsilon}{H^{1/\Delta}}\right). \tag{11}$$

Here f and g are two scaling functions. Figures 12(a)-(b) show  $-\Delta S_M/H^{(1-\alpha)/\Delta}$  vs.  $\epsilon/H^{1/\Delta}$  for  $H \parallel c$ -axis and  $H \parallel ab$ -plane, respectively. This scaled equation of state suggests that, with the correct critical exponents, all rescaled curves under different fields and temperatures should converge into two universal curves when the field is applied along two directions. The accurate collapse and superimposition of these curves validate the credibility of the critical exponents estimated by analyzing the magnetocaloric effects.

The estimated critical exponent values are listed in Table I along with other theoretical and experimental values. Taroni *et al.* have shown that for 2D magnets the critical exponent  $\beta$  is within a range of  $0.1 \le \beta \le 0.25^{65}$ . Our estimated  $\beta$  value lying in this range indicates that  $Cr_2Te_3$  might behave like a 2D magnetic material. We also find that  $\beta$  is very close to that of the tri-critical meanfield model, while  $\gamma$  value approaches the 2D-Ising model value. All these imply this  $Cr_2Te_3$  cannot be simply described as the 2D-Ising type system because multiple magnetic interactions are present in this material.

We can use the critical exponents to estimate the range of magnetic exchange interaction in  $Cr_2Te_3$ . For a homogeneous magnet, the universality class of the magnetic phase transition is contingent on the exchange distance J(r). Theoretically, Fisher *et al.* considered this type of magnetic ordering as an attractive interaction of spins<sup>66</sup>. A renormalization group theory analysis indicates that the

magnetic interactions decay with distance r as  $J(r) \sim 1/r^{(d+\sigma)}$ , where d is the spatial dimensionality, and  $\sigma > 0$ . Moreover, the critical exponents  $\gamma$  can be expressed as following:

$$\gamma = 1 + \frac{4}{d} \left( \frac{n+2}{n+8} \right) \Delta \sigma + \frac{8(n+2)(n-4)}{d^2(n+8)^2} \times \left[ 1 + \frac{2G(d/2)(7n+20)}{(n-4)(n+8)} \right] \Delta \sigma^2$$
 (12)

Here  $G\left(\frac{d}{2}\right)=3-\frac{1}{4}\left(\frac{d}{2}\right)^2$ ,  $\Delta\sigma=\sigma-d/2$ , and n is the spin dimensionality. Using spatial dimension d=2 in equation (12), our estimated  $\sigma$  values are 1.5403, 1.4625, and 1.4267 for the spin dimensionality n=1,2, and 3, respectively. From the correlation length critical exponent  $\upsilon=\gamma/\sigma$  we estimate values of the critical exponent  $\alpha=2-\upsilon d\approx-0.1452$ , -0.2592, and -0.3167 for n=1,2, and 3, respectively. Moreover, applying the Rushbrooke inequality relation<sup>60</sup>, we evaluate  $\alpha=-0.1248$  from our estimated  $\beta$  and  $\gamma$  values. This  $\alpha=-0.1248$  value is very close to the above-estimated value of  $\alpha=-0.1452$  for n=1 and d=2.

For the spatial dimension d=3, our computed  $\sigma$  values using equation (12) are 2.1467, 2.2213, and 2.3511 for n=1,2, and 3, respectively. After following the above-mentioned procedure, we calculate  $\alpha=-0.3089$ , -0.2313, and -0.1082 for n=1,2, and 3, respectively. The calculated  $\alpha$  values are not a good match with the calculated  $\alpha=-0.1248$  from Rushbrooke's inequality relation<sup>60</sup> using the critical exponents values estimated from the magnetocaloric effect (MCE). This is a confirmation that critical exponents estimated for Cr<sub>2</sub>Te<sub>3</sub> from MCE are close to those for the 2D magnetic system with spin dimensionality n=1. Moreover, estimated  $\sigma < 2$  shows the existence of a long-range magnetic ordering in this material. As for a 2D system, long-range magnetic ordering exists due to the presence of strong magneto-crystalline anisotropy which can reduce thermal fluctuation<sup>67</sup>.

For Cr<sub>2</sub>Te<sub>3</sub>, *c*-axis is the magnetic easy-axis, as discussed before. For H  $\parallel$  *ab*-plane, the estimated critical exponent values are  $\beta = 0.9091$ ,  $\gamma = 0.6353$ , and  $\delta = 1.6989$ . These values do not fit well with any known theoretical model values (Table I). Moreover, from the Rushbrook's formula, we calculate  $\alpha = 2 - 2\beta - \gamma = -0.4535$  for H  $\parallel$  *ab*-plane. To identify the spatial and spin dimensionality of our sample, we use this  $\gamma = 0.6353$  value in Equation 12 for various combinations of spatial and spin dimensions (such as, d:n = 3:3, 3:2, 3:1, 2:3, 2:2, 2:1), which yield imaginary  $\sigma$  values for all those combinations. Hence, it is not feasible to perform above mentioned analysis on our system from the estimated critical exponent values for H  $\parallel$  *ab*-plane.

Cr<sub>2</sub>Te<sub>3</sub> is not a layered van der Walls (vdW) material like CrI<sub>3</sub><sup>1</sup>, Cr<sub>2</sub>Ge<sub>2</sub>Te<sub>6</sub><sup>1</sup>, etc. For Cr<sub>2</sub>Te<sub>3</sub>, ferromagnetism originates from the magnetic ordering of Cr moments. The neutron diffraction studies show ferromagnetic ordering of Cr magnetic moments along the *c*-axis<sup>29,30</sup>. In this material, there are covalently bonded Cr atoms between layers of Cr-Te atoms, as shown in Figure 1(b) <sup>22,68</sup>. This crystal structure could explain the two-dimensional nature of magnetism of Cr<sub>2</sub>Te<sub>3</sub> as seen in our analysis.

Temperature dependent heat capacity  $C_p$  of a single crystal  $Cr_2Te_3$  sample for different magnetic fields (up to 9 T) applied along its c-axis is shown in Figure 13(a). A sharp  $\lambda$ -type peak is observed

at ~171 K in zero magnetic field  $C_p$  which indicates a paramagnetic to ferromagnetic phase transition. With an increase of the magnetic field, the peak's height is reduced, and the width is broadened. The peak also shifts toward the higher temperature with an increasing magnetic field. The estimated heat capacity change  $\Delta C_p = C_p(T, H) - C_p(T, 0)$  as a function of temperature for different fields is plotted in Figure 13(b). It should be noted that  $\Delta C_p < 0$  for  $T < T_C$  and  $\Delta C_p > 0$  for  $T > T_C$  and it changes rapidly from negative to positive value at  $T_C$ . This rapid upturn shown in Figure 13(b) confirms a paramagnetic to ferromagnetic phase transition in this material<sup>35</sup>. The total entropy S(T, H) can be determined from heat capacity data by the following relation:

$$S(T,H) = \int_0^T \frac{c_P(T,H)}{T} dT \tag{13}$$

Here it is assumed that the lattice and electronic contributions do not dependent on applied magnetic field<sup>69</sup>. In an adiabatic magnetization process, the magnetic entropy change  $\Delta S_M$  should be expressed as  $\Delta S_M(T, H) = \Delta S_M(T, H) - \Delta S_M(T, 0)$ .

Next, we are going to estimate the adiabatic temperature change  $\Delta T_{ad}$  for various temperatures around the magnetic phase transition. The adiabatic temperature change is defined as change of temperature of a material during the adiabatic magnetization/demagnetization process. The adiabatic temperature change due to the change of magnetic field can be estimated from the following relation:  $\Delta T_{ad}(S,H) = T(S,H) - T(S,0)$ , where T(S,H) and T(S,0) are the temperatures in the field  $H \neq 0$  and H = 0, respectively, at a constant entropy<sup>34</sup>. Figures 13(c)-(d) show temperature-dependent  $\Delta T_{ad}$  and  $-\Delta S_M$ , respectively, determined from heat capacity data for various applied fields. All these curves reach the maximum near the Curie temperature and increase with the increasing magnetic field. In Figure 13(c), with the increase of the magnetic field,  $\Delta T_{ad}$  curves have broadened and their peaks have shifted to higher temperatures just like temperature-dependent specific heat graphs. It is worth noting that peaks of  $\Delta T_{ad}$  curves have shifted from 171 K at 1 T to 175 K at 9 T magnetic field. The maximum of  $-\Delta S_M$  and  $\Delta T_{ad}$  curves are 5.25 J kg<sup>-1</sup> K<sup>-1</sup> (whereas 4.5 J kg<sup>-1</sup> K<sup>-1</sup> from isothermal magnetization) and 3.31 K, respectively, for 9 T applied magnetic field.

#### **Conclusion**

In summary, we have systematically studied the anisotropic magnetocaloric effects (MCE) of single crystal  $Cr_2Te_3$ . We have grown these  $Cr_2Te_3$  samples by CVT and characterized by synchrotron x-ray diffraction. The second-order nature of the paramagnetic-to-ferromagnetic phase transition near  $T_C \approx 170$  K has been verified by the scaling analysis of magnetocaloric effect. The critical exponents  $\beta$ ,  $\gamma$ , and  $\delta$  are estimated by analyzing the magnetocaloric effect, and the scaling analysis of temperature and field-dependent magnetic entropy change confirms the accuracy of our estimated critical exponents. A large magneto-crystalline anisotropy constant  $K_u$  is estimated to be 580.1196 kJ m<sup>-3</sup> at 146 K. Using the heat capacity measurements, we estimate adiabatic temperature  $\Delta T_{ad} = 3.53$  K for 9 T magnetic field. Our analysis shows that  $Cr_2Te_3$  behaves like a 2D Ising system with long-range magnetic ordering.

### \*Supporting Information

Results of refined fractional coordinates (Table S1), occupancies of Cr and Te sites (Table S1), isotropic thermal displacement parameters (Table S1), and Rietveld refinement fitting parameters (Table S2).

#### **Acknowledgements**

This work is supported by the National Science Foundation Awards No. DMR-2018579 and No. DMR-2302436. This work made use of the synthesis facility of the Platform for the Accelerated Realization, Analysis, and Discovery of Interface Materials (PARADIM), which is supported by the National Science Foundation under Cooperative Agreement No. DMR-2039380. This research used beamline 28-ID-1 of the National Synchrotron Light Source-II, a U.S. Department of Energy (DOE) Office of Science User Facility operated for the DOE Office of Science by Brookhaven National Laboratory under Contract No. DE-SC0012704.

Table I: Estimated critical exponent values of Cr<sub>2</sub>Te<sub>3</sub>, including other experimental and theoretical critical exponent values.

Composition	Techniques	β	γ	δ
Cr <sub>2</sub> Te <sub>3</sub> (this work)	Magnetocaloric Effect (MCE)	0.236	1.652	7.994
Theory <sup>70</sup>	Mean-field model	0.5	1	3
Theory <sup>71</sup>	3D Heisenberg model	0.365	1.386	4.82
Theory <sup>71</sup>	3D XY model	0.345	1.361	4.81
Theory <sup>71</sup>	3D Ising model	0.325	1.24	4.80
Theory <sup>71</sup>	Tri-critical mean field model	0.25	1	5
Theory <sup>72</sup>	2D Ising model	0.125	1.75	15
Cr <sub>5</sub> Te <sub>6</sub> <sup>16</sup>	Kouvel-Fisher plot	0.406	1.199	3.99
Cr <sub>4</sub> Te <sub>5</sub> <sup>20</sup>	Kouvel-Fisher plot	0.387	1.287	4.32
$Cr_{0.62}Te^{17}$	Kouvel-Fisher plot	0.315	1.81	6.75
Cr <sub>5</sub> Te <sub>8</sub> <sup>18</sup>	Kouvel-Fisher plot	0.321	1.27	4.9

#### **References:**

- (1) Gong, C.; Li, L.; Li, Z.; Ji, H.; Stern, A.; Xia, Y.; Cao, T.; Bao, W.; Wang, C.; Wang, Y.; Qiu, Z. Q.; Cava, R. J.; Louie, S. G.; Xia, J.; Zhang, X. Discovery of Intrinsic Ferromagnetism in Two-Dimensional van Der Waals Crystals. *Nature* **2017**, *546* (7657), 265–269. https://doi.org/10.1038/nature22060.
- (2) Wang, M.-C.; Huang, C.-C.; Cheung, C.-H.; Chen, C.-Y.; Tan, S. G.; Huang, T.-W.; Zhao, Y.; Zhao, Y.; Wu, G.; Feng, Y.-P.; Wu, H.-C.; Chang, C.-R. Prospects and Opportunities of 2D van Der Waals Magnetic Systems. *Ann Phys* **2020**, *532* (5), 1900452. https://doi.org/https://doi.org/10.1002/andp.201900452.
- (3) Zhang, W.; Wong, P. K. J.; Zhu, R.; Wee, A. T. S. Van Der Waals Magnets: Wonder Building Blocks for Two-Dimensional Spintronics? *InfoMat* **2019**, *1* (4), 479–495. https://doi.org/https://doi.org/10.1002/inf2.12048.
- (4) Ningrum, V. P.; Liu, B.; Wang, W.; Yin, Y.; Cao, Y.; Zha, C.; Xie, H.; Jiang, X.; Sun, Y.; Qin, S.; Chen, X.; Qin, T.; Zhu, C.; Wang, L.; Huang, W. Recent Advances in Two-Dimensional Magnets: Physics and Devices towards Spintronic Applications. *Research* **2023**, *2020*. https://doi.org/10.34133/2020/1768918.
- (5) Tong, Q.; Liu, F.; Xiao, J.; Yao, W. Skyrmions in the Moiré of van Der Waals 2D Magnets. *Nano Lett* **2018**, *18* 11, 7194–7199.
- (6) Li, Y.; Yang, B.; Xu, S.; Huang, B.; Duan, W. Emergent Phenomena in Magnetic Two-Dimensional Materials and van Der Waals Heterostructures. *ACS Appl Electron Mater* **2022**, *4* (7), 3278–3302. https://doi.org/10.1021/acsaelm.2c00419.
- (7) Gibertini, M.; Koperski, M.; Morpurgo, A. F.; Novoselov, K. S. Magnetic 2D Materials and Heterostructures. *Nat Nanotechnol* **2019**, *14* (5), 408–419. https://doi.org/10.1038/s41565-019-0438-6.
- (8) Eto, T.; Ishizuka, M.; Endo, S.; Kanomata, T.; Kikegawa, T. Pressure-Induced Structural Phase Transition in a Ferromagnet CrTe. *J Alloys Compd* **2001**, *315* (1), 16–21. https://doi.org/https://doi.org/10.1016/S0925-8388(00)01237-8.
- (9) Freitas, D. C.; Weht, R.; Sulpice, A.; Remenyi, G.; Strobel, P.; Gay, F.; Marcus, J.; Núñez-Regueiro, M. Ferromagnetism in Layered Metastable 1T-CrTe2. *Journal of Physics: Condensed Matter* 2015, 27 (17), 176002. https://doi.org/10.1088/0953-8984/27/17/176002.
- (10) Zhang, X.; Lu, Q.; Liu, W.; Niu, W.; Sun, J.; Cook, J.; Vaninger, M.; Miceli, P. F.; Singh, D. J.; Lian, S.-W.; Chang, T.-R.; He, X.; Du, J.; He, L.; Zhang, R.; Bian, G.; Xu, Y. Room-Temperature Intrinsic Ferromagnetism in Epitaxial CrTe2 Ultrathin Films. *Nat Commun* 2021, 12 (1), 2492. https://doi.org/10.1038/s41467-021-22777-x.
- (11) Wang, F.; Du, J.; Sun, F.; Sabirianov, R. F.; Al-Aqtash, N.; Sengupta, D.; Zeng, H.; Xu, X. Ferromagnetic Cr2Te3 Nanorods with Ultrahigh Coercivity. *Nanoscale* **2018**, *10* (23), 11028–11033. https://doi.org/10.1039/C8NR02272K.
- (12) Pramanik, T.; Roy, A.; Dey, R.; Rai, A.; Guchhait, S.; Movva, H. C. P.; Hsieh, C.-C.; Banerjee, S. K. Angular Dependence of Magnetization Reversal in Epitaxial Chromium Telluride Thin Films with

- Perpendicular Magnetic Anisotropy. *J Magn Magn Mater* **2017**, *437*, 72–77. https://doi.org/https://doi.org/10.1016/j.jmmm.2017.04.039.
- (13) Roy, A.; Guchhait, S.; Dey, R.; Pramanik, T.; Hsieh, C.-C.; Rai, A.; Banerjee, S. K. Perpendicular Magnetic Anisotropy and Spin Glass-like Behavior in Molecular Beam Epitaxy Grown Chromium Telluride Thin Films. *ACS Nano* **2015**, *9* (4), 3772–3779. https://doi.org/10.1021/nn5065716.
- (14) Wen, Y.; Liu, Z.; Zhang, Y.; Xia, C.; Zhai, B.; Zhang, X.; Zhai, G.; Shen, C.; He, P.; Cheng, R.; Yin, L.; Yao, Y.; Getaye Sendeku, M.; Wang, Z.; Ye, X.; Liu, C.; Jiang, C.; Shan, C.; Long, Y.; He, J. Tunable Room-Temperature Ferromagnetism in Two-Dimensional Cr2Te3. *Nano Lett* **2020**, *20* (5), 3130–3139. https://doi.org/10.1021/acs.nanolett.9b05128.
- (15) Wang, Y.; Kajihara, S.; Matsuoka, H.; Saika, B. K.; Yamagami, K.; Takeda, Y.; Wadati, H.; Ishizaka, K.; Iwasa, Y.; Nakano, M. Layer-Number-Independent Two-Dimensional Ferromagnetism in Cr3Te4. *Nano Lett* **2022**, *22* (24), 9964–9971. https://doi.org/10.1021/acs.nanolett.2c03532.
- (16) Zhang, L.-Z.; Xiao, Q.-L.; Chen, F.; Feng, Z.; Cao, S.; Zhang, J.; Ge, J.-Y. Multiple Magnetic Phase Transitions and Critical Behavior in Single Crystal Cr5Te6. *J Magn Magn Mater* **2022**, *546*, 168770. https://doi.org/https://doi.org/10.1016/j.jmmm.2021.168770.
- (17) Liu, Y.; Petrovic, C. Critical Behavior of the Quasi-Two-Dimensional Weak Itinerant Ferromagnet Trigonal Chromium Telluride \${\mathrm{Cr}}\_{0.62}\mathrm{Te}\$. *Phys Rev B* **2017**, *96* (13), 134410. https://doi.org/10.1103/PhysRevB.96.134410.
- (18) Zhang, X.; Yu, T.; Xue, Q.; Lei, M.; Jiao, R. Critical Behavior and Magnetocaloric Effect in Monoclinic Cr5Te8. *J Alloys Compd* **2018**, *750*, 798–803. https://doi.org/https://doi.org/10.1016/j.jallcom.2018.03.318.
- (19) Mondal, R.; Kulkarni, R.; Thamizhavel, A. Anisotropic Magnetic Properties and Critical Behaviour Studies of Trigonal Cr5Te8 Single Crystal. *J Magn Magn Mater* **2019**, *483*, 27–33. https://doi.org/https://doi.org/10.1016/j.jmmm.2019.02.082.
- Zhang, L.-Z.; Zhang, A.-L.; He, X.-D.; Ben, X.-W.; Xiao, Q.-L.; Lu, W.-L.; Chen, F.; Feng, Z.; Cao, S.; Zhang, J.; Ge, J.-Y. Critical Behavior and Magnetocaloric Effect of the Quasi-Two-Dimensional Room-Temperature Ferromagnet \$\mathrm{Cr}{}\_{4}\mathrm{Te}{}\_{5}\$. *Phys Rev B* **2020**, *101* (21), 214413. https://doi.org/10.1103/PhysRevB.101.214413.
- (21) Ipser, H.; Komarek, K. L.; Klepp, K. O. Transition Metal-Chalcogen Systems Viii: The CraTe Phase Diagram. *Journal of the Less Common Metals* **1983**, *92* (2), 265–282. https://doi.org/https://doi.org/10.1016/0022-5088(83)90493-9.
- (22) Dijkstra, J.; Weitering, H. H.; Bruggen, C. F. Van.; Haas, C.; Groot, R. A. De. Band-Structure Calculations, and Magnetic and Transport Properties of Ferromagnetic Chromium Tellurides (CrTe, Cr3Te4, Cr2Te3). *Journal of Physics: Condensed Matter* **1989**, *1* (46), 9141. https://doi.org/10.1088/0953-8984/1/46/008.
- (23) Hamad, M. Kh.; Nlebedim, I. C.; Maswadeh, Y.; Hamad, R.; Ziq, Kh. A. Room Temperature Magnetocaloric Effect in CrTe1–xSex Alloys. *The European Physical Journal Plus* **2022**, *137* (11), 1259. https://doi.org/10.1140/epjp/s13360-022-03487-9.

- (24) Hamad, M. Kh.; Nlebedim, I. C.; Ziq, K. A. Evaluation of the Critical Behavior near Ferromagnetic to Paramagnetic Phase Transition in CrTe1-XSex Alloys: An Experimental Study. *Physica B Condens Matter* **2023**, *665*, 415072. https://doi.org/10.1016/j.physb.2023.415072.
- (25) Hashimoto, T.; Hoya, K.; Yamaguchi, M.; Ichitsubo, I. Magnetic Properties of Single Crystals Cr2-ΔTe3. *J Physical Soc Japan* **1971**, *31* (3), 679–682. https://doi.org/10.1143/JPSJ.31.679.
- (26) Sato, K.; Aman, Y.; Hirai, M.; Fujisawa, M. Reflectivity Spectra in Single Crystals of Cr3Te4, Cr2Te3 and Cr2Se3 between 0.3 and 23 EV. *J Physical Soc Japan* **1990**, *59* (2), 435–438. https://doi.org/10.1143/JPSJ.59.435.
- (27) Andresen, A. F.; Zeppezauer, E.; Boive, T.; Nordström, B.; Brändén, C. I. The Magnetic Structure of Cr2Te3, Cr3Te4, and Cr5Te6. *Acta Chem Scand* **1970**, *24*, 3495–3509.
- (28) Youn, S. J.; Kwon, S. K.; Min, B. I. Correlation Effect and Magnetic Moments in Cr2Te3. *J Appl Phys* **2007**, *101* (9), 09G522. https://doi.org/10.1063/1.2713699.
- (29) Hamasaki, T.; Hashimoto, T.; Yamaguchi, Y.; Watanabe, H. Neutron Diffraction Study of Cr2Te3 Single Crystal. *Solid State Commun* **1975**, *16* (7), 895–897. https://doi.org/https://doi.org/10.1016/0038-1098(75)90888-1.
- (30) Andresen, A. F.; Rasmussen, S. E.; Hirvisalo, E. L.; Munch-Petersen, J. A NEUTRON DIFFRACTION INVESTIGATION OF Cr\$sub 2\$Te\$sub 3\$ AND Cr\$sub 5\$Te\$sub 6\$. *Acta Chem Scand* **1963**, *17*, 1335–1342.
- (31) John B. Goodenough: Magnetism and the Chemical Bond; interscience: New York, 1963; Vol. I.
- (32) Gschneidner Jr., K. A.; Pecharsky, V. K.; Pecharsky, A. O.; Zimm, C. B. Recent Developments in Magnetic Refrigeration. *Materials Science Forum* 1999, 315–317, 69–76. https://doi.org/10.4028/www.scientific.net/MSF.315-317.69.
- (33) Pecharsky, V. K.; Gschneidner Jr, K. A. Magnetocaloric Effect and Magnetic Refrigeration. *J Magn Magn Mater* **1999**, *200* (1), 44–56. https://doi.org/https://doi.org/10.1016/S0304-8853(99)00397-2.
- (34) Franco, V.; Blázquez, J. S.; Ingale, B.; Conde, A. The Magnetocaloric Effect and Magnetic Refrigeration Near Room Temperature: Materials and Models. *Annu Rev Mater Res* **2012**, *42* (1), 305–342. https://doi.org/10.1146/annurev-matsci-062910-100356.
- (35) Liu, Y.; Petrovic, C. Anisotropic Magnetocaloric Effect in Single Crystals of \${\mathrm{CrI}}\_{3}\$. *Phys Rev B* **2018**, *97* (17), 174418. https://doi.org/10.1103/PhysRevB.97.174418.
- (36) Liu, Y.; Petrovic, C. Anisotropic Magnetocaloric Effect and Critical Behavior in \${\mathrm{CrCl}}\_{3}\$. *Phys Rev B* **2020**, *102* (1), 14424. https://doi.org/10.1103/PhysRevB.102.014424.
- (37) Mondal, S.; Midya, A.; Patidar, M. M.; Ganesan, V.; Mandal, P. Magnetic and Magnetocaloric Properties of Layered van Der Waals CrCl3. Appl Phys Lett 2020, 117 (9), 092405. https://doi.org/10.1063/5.0019985.

- (38) Liu, Y.; Hu, Z.; Petrovic, C. Anisotropic Magnetocaloric Effect and Critical Behavior in \${\mathrm{CrSbSe}}\_{3}\$. *Phys Rev B* **2020**, *102* (1), 14425. https://doi.org/10.1103/PhysRevB.102.014425.
- (39) Liu, W.; Dai, Y.; Yang, Y.-E.; Fan, J.; Pi, L.; Zhang, L.; Zhang, Y. Critical Behavior of the Single-Crystalline van Der Waals Bonded Ferromagnet \${\mathrm{Cr}}\_{2}{\mathrm{Ge}}\_{2}{\mathrm{Te}}\_{6}\$. Phys Rev B **2018**, 98 (21), 214420. https://doi.org/10.1103/PhysRevB.98.214420.
- (40) Toby, B. H.; Von Dreele, R. B. GSAS-II: The Genesis of a Modern Open-Source All Purpose Crystallography Software Package. *J Appl Crystallogr* **2013**, *46* (2), 544–549. https://doi.org/https://doi.org/10.1107/S0021889813003531.
- (41) Bensch, W.; Helmer, O.; Näther, C. Determination and Redetermination of the Crystal Structures of Chromium Tellurides in the Composition Range CrTe1.56–CrTe1.67: Trigonal Di-Chromium Tri-Telluride Cr2Te3, Monoclinic Penta-Chromium Octa-Telluride Cr5Te8, and the Five Layer Superstructure of Trigonal Penta-Chromium Octa-Telluride Cr5Te8. *Mater Res Bull* 1997, 32 (3), 305–318. https://doi.org/https://doi.org/10.1016/S0025-5408(96)00194-8.
- (42) Liu, Y.; Petrovic, C. Anomalous Hall Effect in the Trigonal \${\mathrm{Cr}}\_{5}{\mathrm{Te}}\_{8}\$ Single Crystal. *Phys Rev B* **2018**, *98* (19), 195122. https://doi.org/10.1103/PhysRevB.98.195122.
- (43) Kieffer, J.; Valls, V.; Blanc, N.; Hennig, C. New Tools for Calibrating Diffraction Setups. *J Synchrotron Radiat* **2020**, *27* (2), 558–566. https://doi.org/10.1107/S1600577520000776.
- (44) Tian, C.-K.; Wang, C.; Ji, W.; Wang, J.-C.; Xia, T.-L.; Wang, L.; Liu, J.-J.; Zhang, H.-X.; Cheng, P. Domain Wall Pinning and Hard Magnetic Phase in Co-Doped Bulk Single Crystalline \${\mathrm{Fe}}\_{3}{\mathrm{GeTe}}\_{2}\$. Phys Rev B **2019**, 99 (18), 184428. https://doi.org/10.1103/PhysRevB.99.184428.
- (45) Casto, L. D.; Clune, A. J.; Yokosuk, M. O.; Musfeldt, J. L.; Williams, T. J.; Zhuang, H. L.; Lin, M.-W.; Xiao, K.; Hennig, R. G.; Sales, B. C.; Yan, J.-Q.; Mandrus, D. Strong Spin-Lattice Coupling in CrSiTe3. *APL Mater* **2015**, *3* (4), 041515. https://doi.org/10.1063/1.4914134.
- (46) Richter, N.; Weber, D.; Martin, F.; Singh, N.; Schwingenschlögl, U.; Lotsch, B. V; Kläui, M. Temperature-Dependent Magnetic Anisotropy in the Layered Magnetic Semiconductors \$\mathrm{Cr}{\mathrm{I}}\_{3}\$ and \$\mathrm{CrB}{\mathrm{r}}\_{3}\$. *Phys Rev Mater* **2018**, *2* (2), 24004. https://doi.org/10.1103/PhysRevMaterials.2.024004.
- (47) Liu, Y.; Abeykoon, M.; Stavitski, E.; Attenkofer, K.; Petrovic, C. Magnetic Anisotropy and Entropy Change in Trigonal \${\mathrm{Cr}}\_{5}{\mathrm{Te}}\_{8}\$. Phys Rev B **2019**, 100 (24), 245114. https://doi.org/10.1103/PhysRevB.100.245114.
- (48) Wang, Y.; Yan, J.; Li, J.; Wang, S.; Song, M.; Song, J.; Li, Z.; Chen, K.; Qin, Y.; Ling, L.; Du, H.; Cao, L.; Luo, X.; Xiong, Y.; Sun, Y. Magnetic Anisotropy and Topological Hall Effect in the Trigonal Chromium Tellurides \${\mathrm{Cr}}\_{5}{\mathrm{Te}}\_{8}\$. *Phys Rev B* **2019**, *100* (2), 24434. https://doi.org/10.1103/PhysRevB.100.024434.

- (49) Zhong, Y.; Peng, C.; Huang, H.; Guan, D.; Hwang, J.; Hsu, K. H.; Hu, Y.; Jia, C.; Moritz, B.; Lu, D.; Lee, J.-S.; Jia, J.-F.; Devereaux, T. P.; Mo, S.-K.; Shen, Z.-X. From Stoner to Local Moment Magnetism in Atomically Thin Cr2Te3. *Nat Commun* **2023**, *14* (1), 5340. https://doi.org/10.1038/s41467-023-40997-1.
- (50) Cullity, B. D.; Graham, C. D. *Introduction to Magnetic Materials*, 2nd ed.; Wiley, 2008. https://doi.org/10.1002/9780470386323.
- (51) Yan, J.; Luo, X.; Chen, F. C.; Gao, J. J.; Jiang, Z. Z.; Zhao, G. C.; Sun, Y.; Lv, H. Y.; Tian, S. J.; Yin, Q. W.; Lei, H. C.; Lu, W. J.; Tong, P.; Song, W. H.; Zhu, X. B.; Sun, Y. P. Anisotropic Magnetic Entropy Change in the Hard Ferromagnetic Semiconductor \$\mathrm{V}{\mathrm{I}}\_{3}\$. *Phys Rev B* **2019**, *100* (9), 94402. https://doi.org/10.1103/PhysRevB.100.094402.
- (52) Zener, C. Classical Theory of the Temperature Dependence of Magnetic Anisotropy Energy. *Physical Review* **1954**, *96* (5), 1335–1337. https://doi.org/10.1103/PhysRev.96.1335.
- (53) Carr, W. J. Temperature Dependence of Ferromagnetic Anisotropy. *Physical Review* **1958**, *109* (6), 1971–1976. https://doi.org/10.1103/PhysRev.109.1971.
- (54) Amaral, J. S.; Reis, M. S.; Amaral, V. S.; Mendonça, T. M.; Araújo, J. P.; Sá, M. A.; Tavares, P. B.; Vieira, J. M. Magnetocaloric Effect in Er- and Eu-Substituted Ferromagnetic La-Sr Manganites. *J Magn Magn Mater* **2005**, *290*–*291*, 686–689. https://doi.org/https://doi.org/10.1016/j.jmmm.2004.11.337.
- (55) Franco, V.; Conde, A. Scaling Laws for the Magnetocaloric Effect in Second Order Phase Transitions: From Physics to Applications for the Characterization of Materials. *International Journal of Refrigeration* **2010**, *33* (3), 465–473. https://doi.org/https://doi.org/10.1016/j.ijrefrig.2009.12.019.
- (56) Liu, Y.; Abeykoon, M.; Petrovic, C. Critical Behavior and Magnetocaloric Effect in \${\mathrm{VI}}\_{3}\$. *Phys Rev Res* **2020**, *2* (1), 13013. https://doi.org/10.1103/PhysRevResearch.2.013013.
- (57) Oesterreicher, H.; Parker, F. T. Magnetic Cooling near Curie Temperatures above 300 K. *J Appl Phys* **1984**, *55* (12), 4334–4338. https://doi.org/10.1063/1.333046.
- (58) Franco, V.; Conde, A.; Romero-Enrique, J. M.; Blázquez, J. S. A Universal Curve for the Magnetocaloric Effect: An Analysis Based on Scaling Relations. *Journal of Physics: Condensed Matter* **2008**, *20* (28), 285207. https://doi.org/10.1088/0953-8984/20/28/285207.
- (59) Franco, V.; Blázquez, J. S.; Conde, A. Field Dependence of the Magnetocaloric Effect in Materials with a Second Order Phase Transition: A Master Curve for the Magnetic Entropy Change. *Appl Phys Lett* **2006**, *89* (22), 222512. https://doi.org/10.1063/1.2399361.
- (60) Stanley, H. E. *Introduction to Phase Transition and Critical Phenomena*; Oxford University press, 1971.
- (61) Fan, J.; Pi, L.; Zhang, L.; Tong, W.; Ling, L.; Hong, B.; Shi, Y.; Zhang, W.; Lu, D.; Zhang, Y. Investigation of Critical Behavior in Pr0.55Sr0.45MnO3 by Using the Field Dependence of

- Magnetic Entropy Change. *Appl Phys Lett* **2011**, *98* (7), 072508. https://doi.org/10.1063/1.3554390.
- (62) Samatham, S. S.; Ganesan, V. Critical Behavior, Universal Magnetocaloric, and Magnetoresistance Scaling of MnSi. *Phys Rev B* **2017**, *95* (11), 115118. https://doi.org/10.1103/PhysRevB.95.115118.
- (63) Widom, B. Equation of State in the Neighborhood of the Critical Point. *J Chem Phys* **2004**, *43* (11), 3898–3905. https://doi.org/10.1063/1.1696618.
- (64) Kadanoff, L. P. Scaling Laws for Ising Models near \${T}\_{c}\$. *Physics Physique Fizika* **1966**, *2* (6), 263–272. https://doi.org/10.1103/PhysicsPhysiqueFizika.2.263.
- (65) Taroni, A.; Bramwell, S. T.; Holdsworth, P. C. W. Universal Window for Two-Dimensional Critical Exponents. *Journal of Physics: Condensed Matter* **2008**, *20* (27), 275233. https://doi.org/10.1088/0953-8984/20/27/275233.
- (66) Fisher, M. E.; Ma, S.; Nickel, B. G. Critical Exponents for Long-Range Interactions. *Phys Rev Lett* **1972**, *29* (14), 917–920. https://doi.org/10.1103/PhysRevLett.29.917.
- (67) Mermin, N. D.; Wagner, H. Absence of Ferromagnetism or Antiferromagnetism in One- or Two-Dimensional Isotropic Heisenberg Models. *Phys Rev Lett* 1966, 17 (22), 1133–1136. https://doi.org/10.1103/PhysRevLett.17.1133.
- (68) Bian, M.; Kamenskii, A. N.; Han, M.; Li, W.; Wei, S.; Tian, X.; Eason, D. B.; Sun, F.; He, K.; Hui, H.; Yao, F.; Sabirianov, R.; Bird, J. P.; Yang, C.; Miao, J.; Lin, J.; Crooker, S. A.; Hou, Y.; Zeng, H. Covalent 2D Cr2Te3 Ferromagnet. *Mater Res Lett* **2021**, *9* (5), 205–212. https://doi.org/10.1080/21663831.2020.1865469.
- (69) Engelbrecht, K.; Bahl, C. R. H.; Nielsen, K. K. Experimental Results for a Magnetic Refrigerator Using Three Different Types of Magnetocaloric Material Regenerators. *International Journal of Refrigeration* 2011, 34 (4), 1132–1140. https://doi.org/https://doi.org/10.1016/j.ijrefrig.2010.11.014.
- (70) Arrott, A. Criterion for Ferromagnetism from Observations of Magnetic Isotherms. *Physical Review* **1957**, *108* (6), 1394–1396. https://doi.org/10.1103/PhysRev.108.1394.
- (71) Kaul, S. N. Static Critical Phenomena in Ferromagnets with Quenched Disorder. *J Magn Magn Mater* **1985**, *53* (1), 5–53. https://doi.org/https://doi.org/10.1016/0304-8853(85)90128-3.
- (72) Le Guillou, J. C.; Zinn-Justin, J. Critical Exponents from Field Theory. *Phys Rev B* **1980**, *21* (9), 3976–3998. https://doi.org/10.1103/PhysRevB.21.3976.

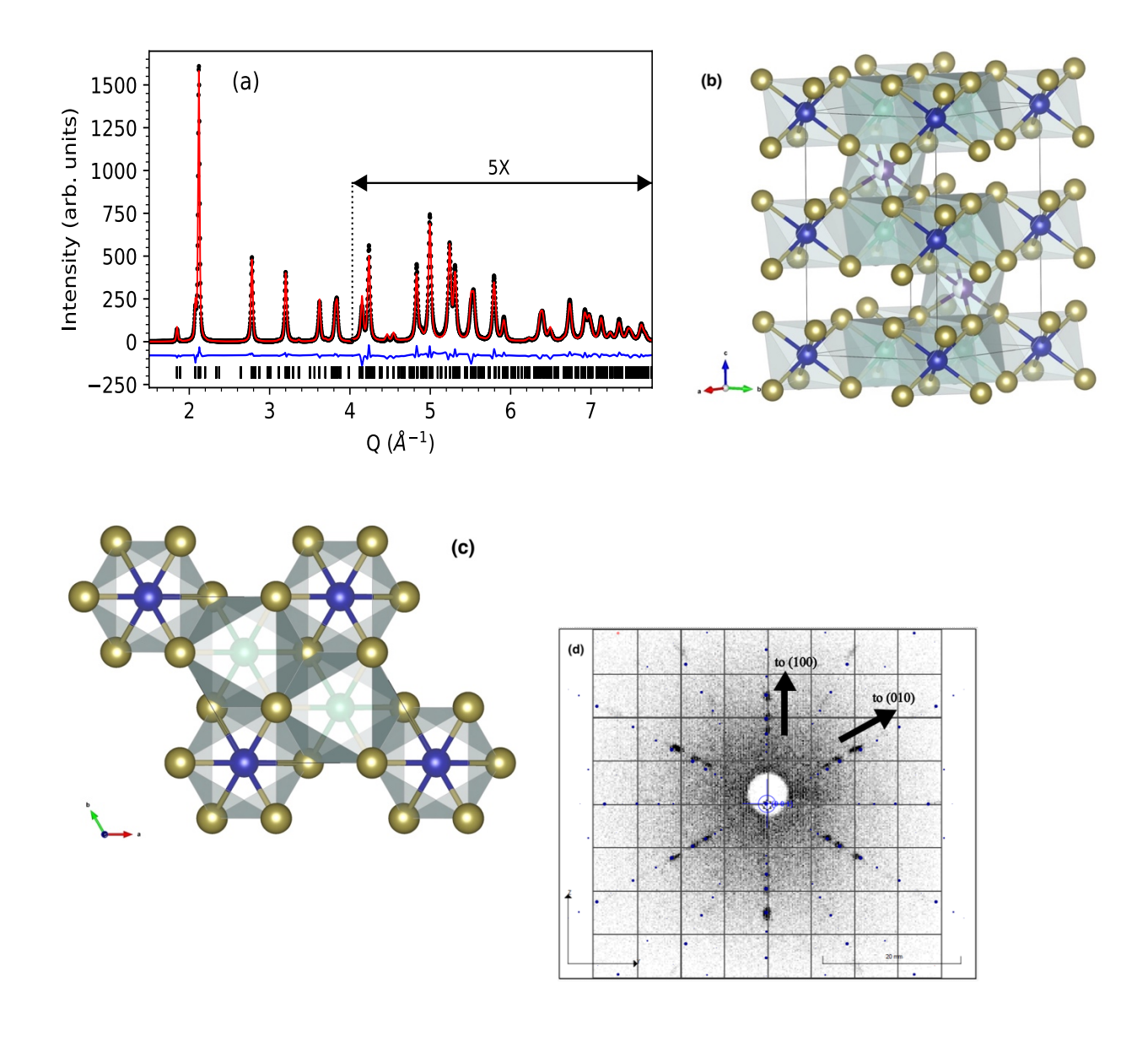


**Figure 1:** (a) Rietveld fit to background subtracted powder diffraction data. Black dots and the red line represent measured and calculated intensities, respectively. A residue plot (blue), and calculated Bragg reflection tick marks are shown below. The observed and calculated intensities, and the fit residue above  $Q \sim 4 \text{ Å}^{-1}$  are multiplied by 5 for clarity. (b) 3-Dimentional, and (c) along crystallographic c-axis polyhedral views of the refined crystallographic unit cell. Blue, green, and half purple half white balls represent, Cr(0, 0, 0) (fully occupied), Cr(0.3333, 0.6667, 0.9968) (fully occupied), and Cr(0.3333, 0.6667, 0.2500) partially occupied sites, respectively. Light green balls represent Te sites. (d) Laue diffraction image of the single crystal

Cr<sub>2</sub>Te<sub>3</sub> sample. The sample is oriented along the crystallographic (001) axis. Arrows show the direction to the other crystallographic axes, as simulated by the QLaue software.

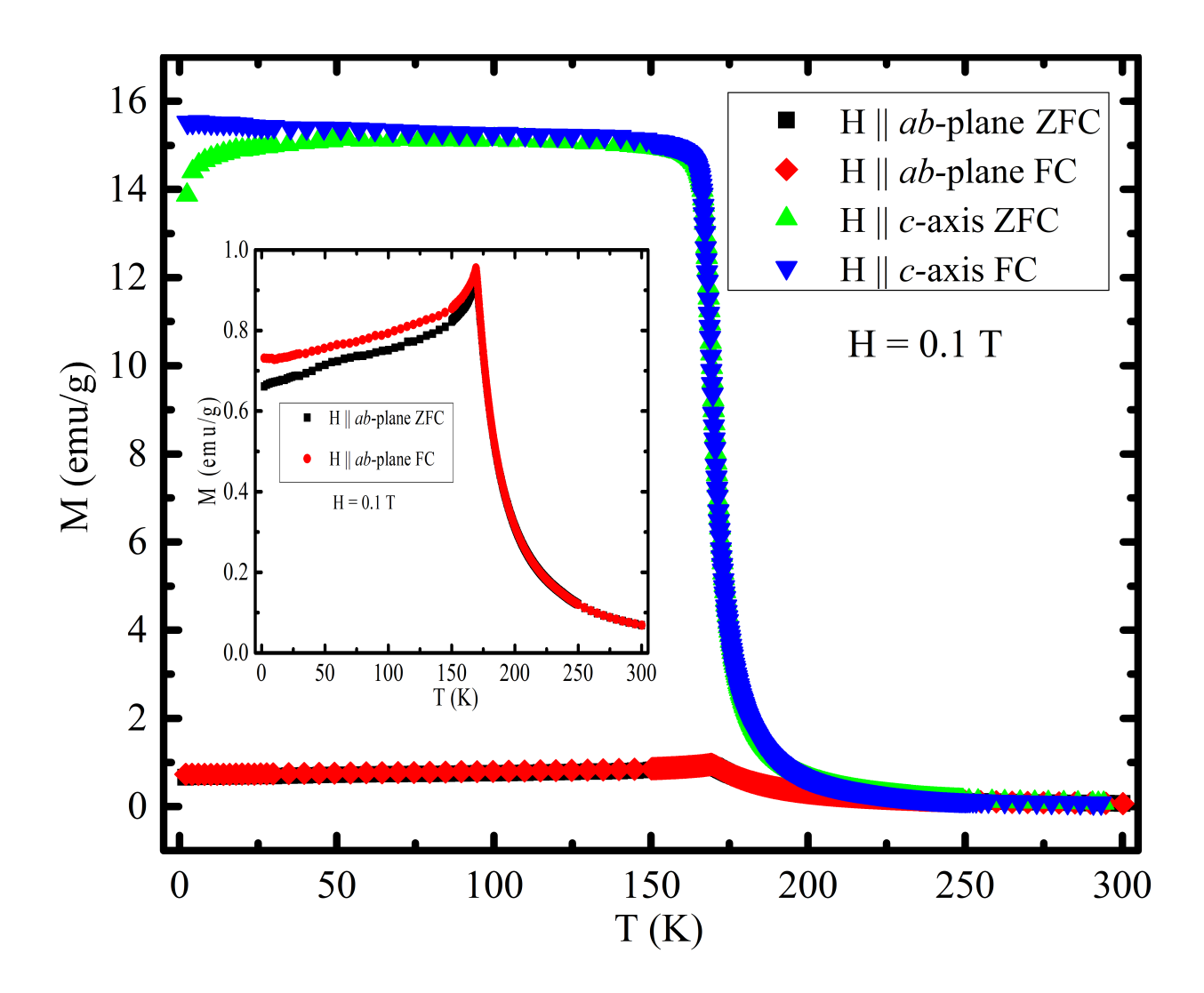
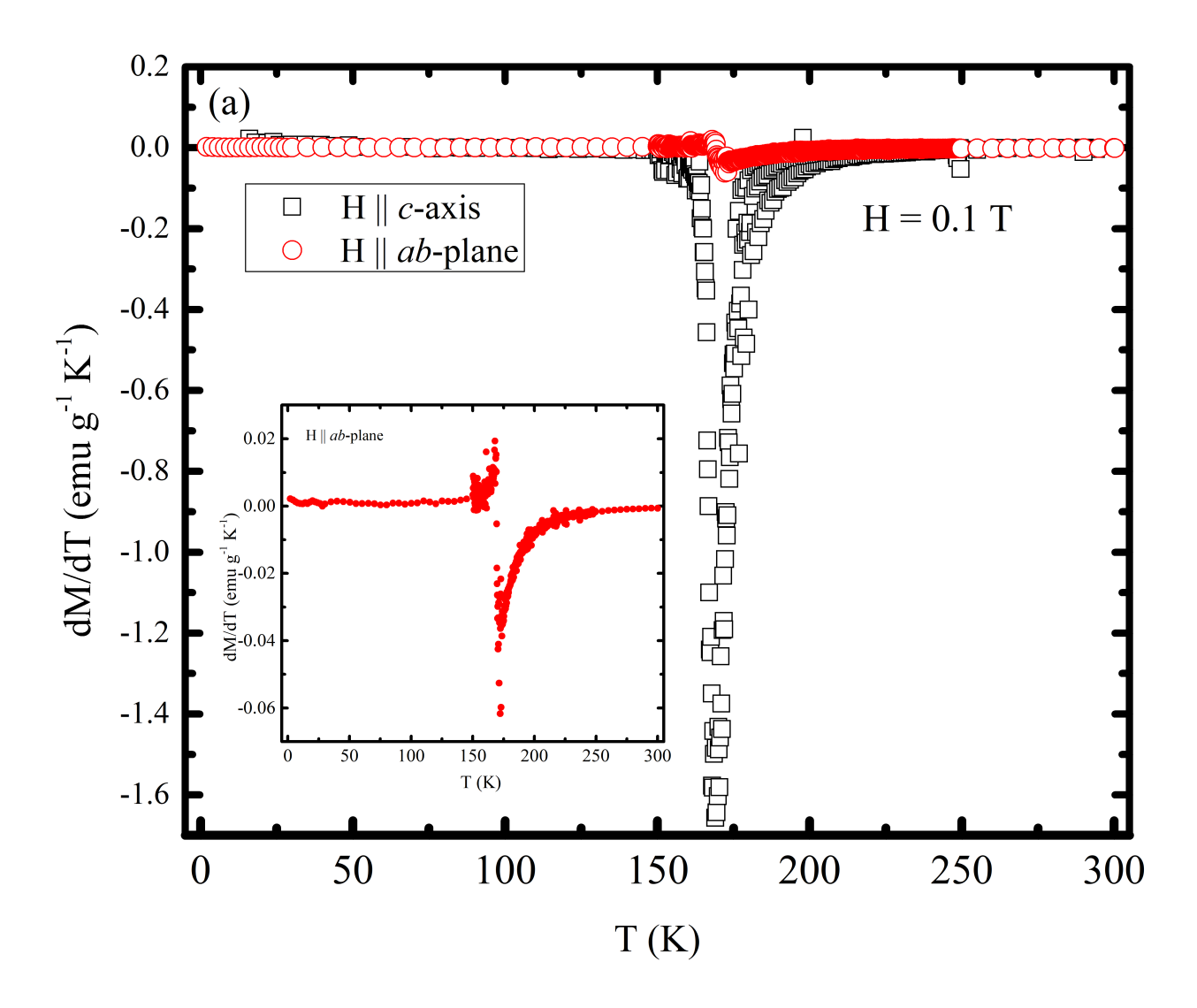


Figure 2: Temperature dependent zero-field-cooled (ZFC) and field-cooled (FC) magnetization for  $0.1~\mathrm{T}$  magnetic field applied along the c-axis (out-of-plane) and ab-plane (in-plane). The inset shows FC and ZFC magnetizations for field along the ab-plane.



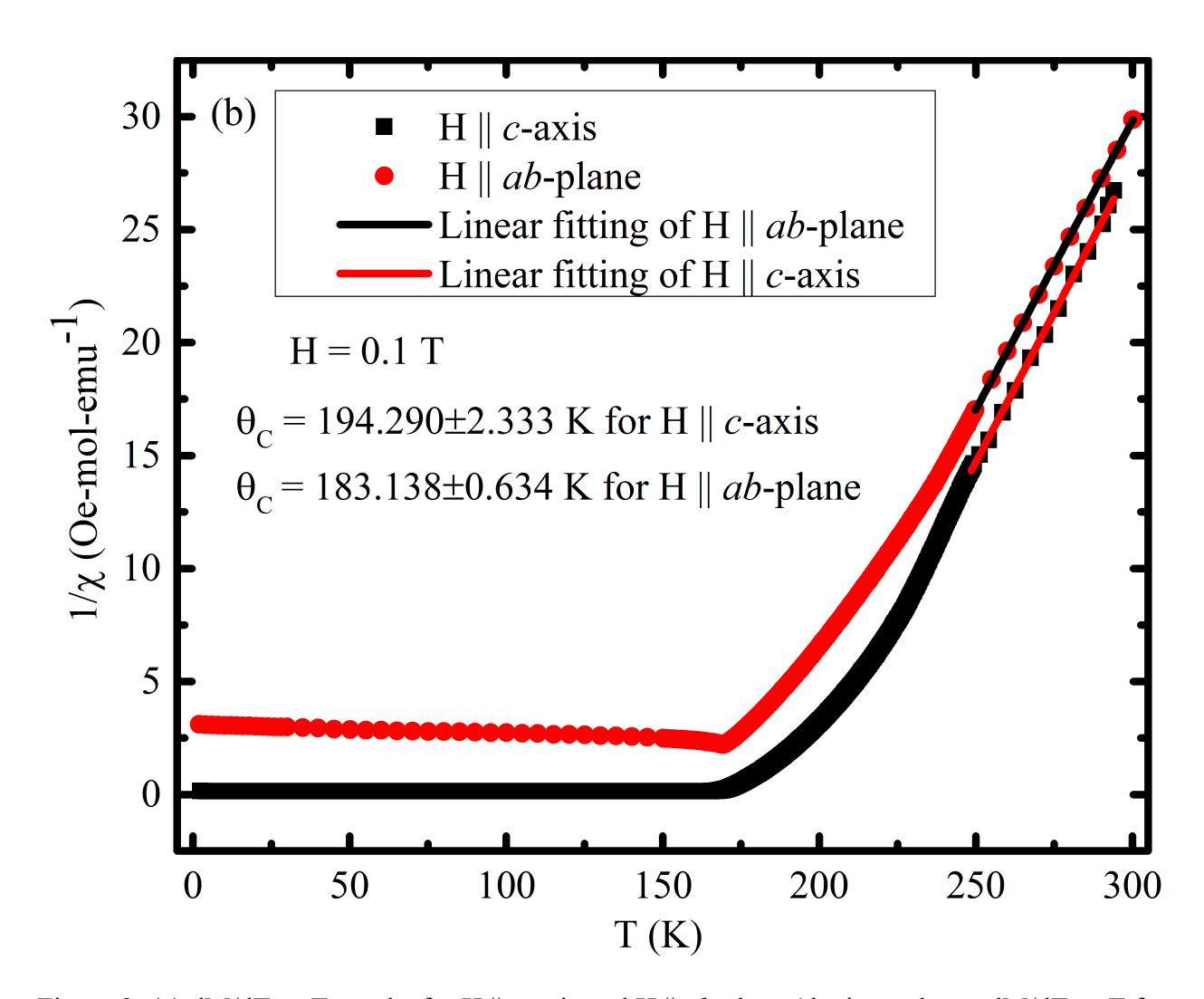


Figure 3: (a) dM/dT vs T graphs for H  $\parallel$  *c*-axis and H  $\parallel$  *ab*-plane (the inset shows dM/dT vs T for H $\parallel$  *ab*-plane for clarity) (b) temperature dependent inverse magnetic susceptibility for H  $\parallel$  *c*-axis and H  $\parallel$  *ab*-plane.

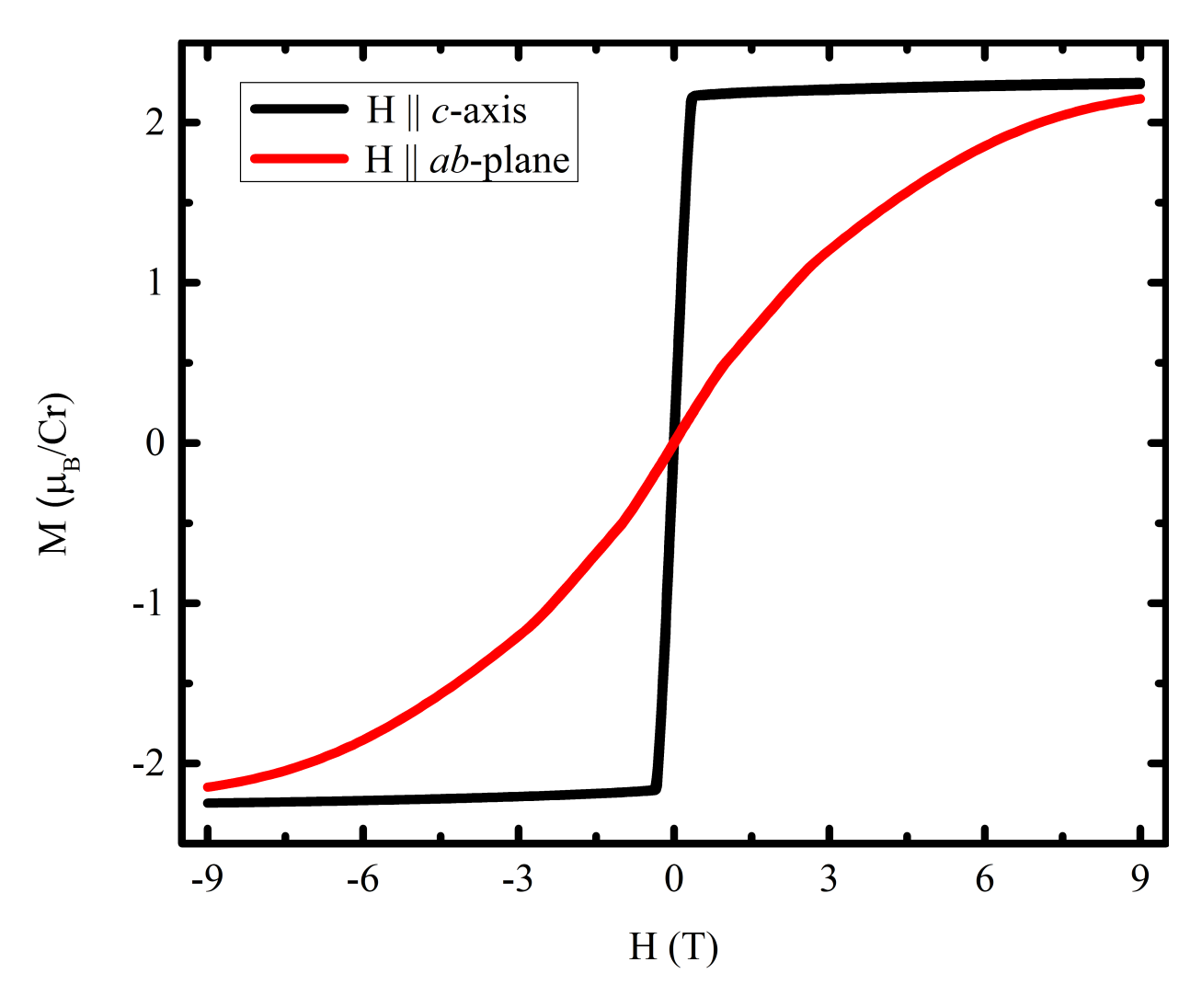
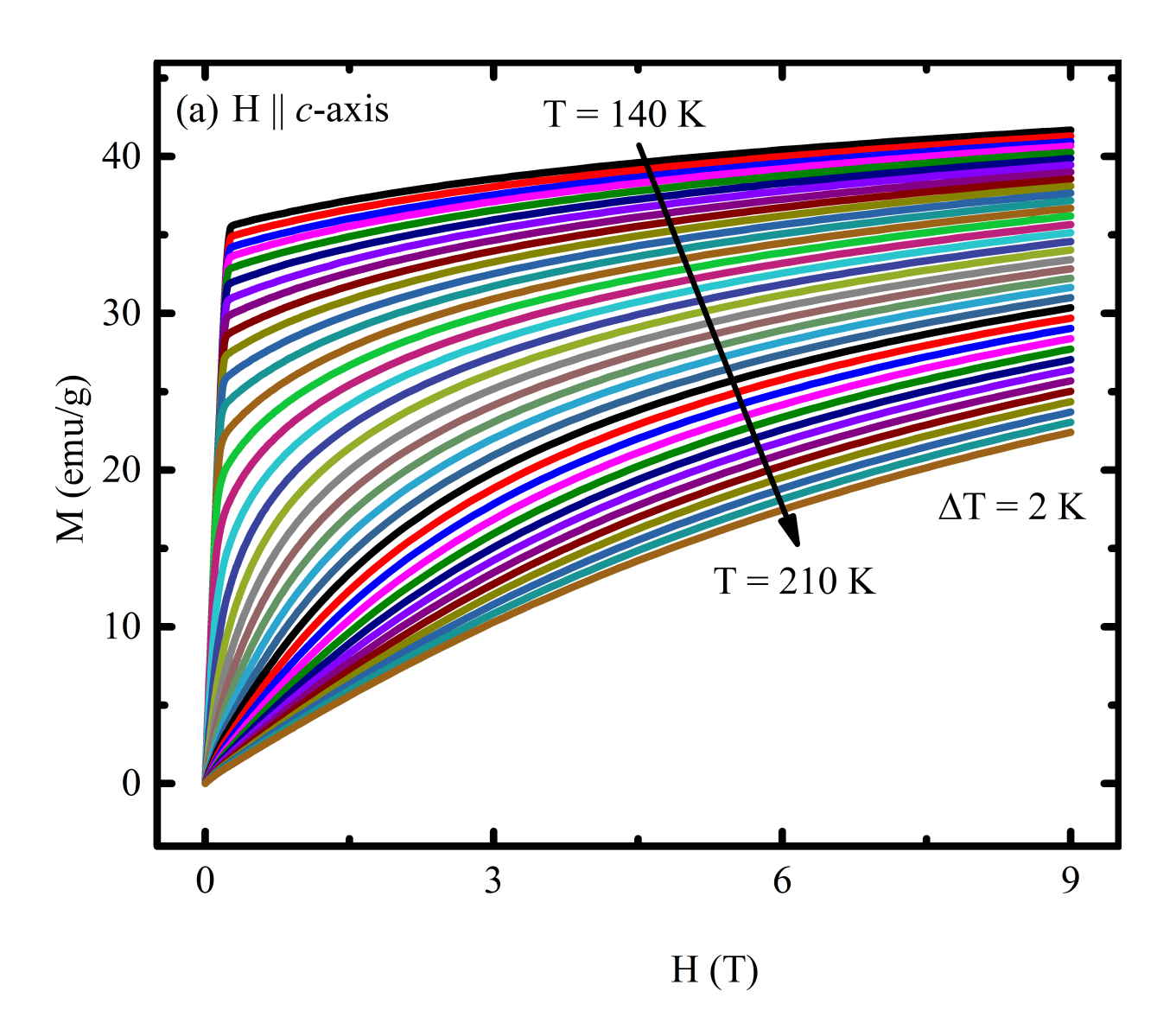


Figure 4: Field dependence of magnetization at 2 K for field applied along the c-axis and ab-plane of a single crystal sample.



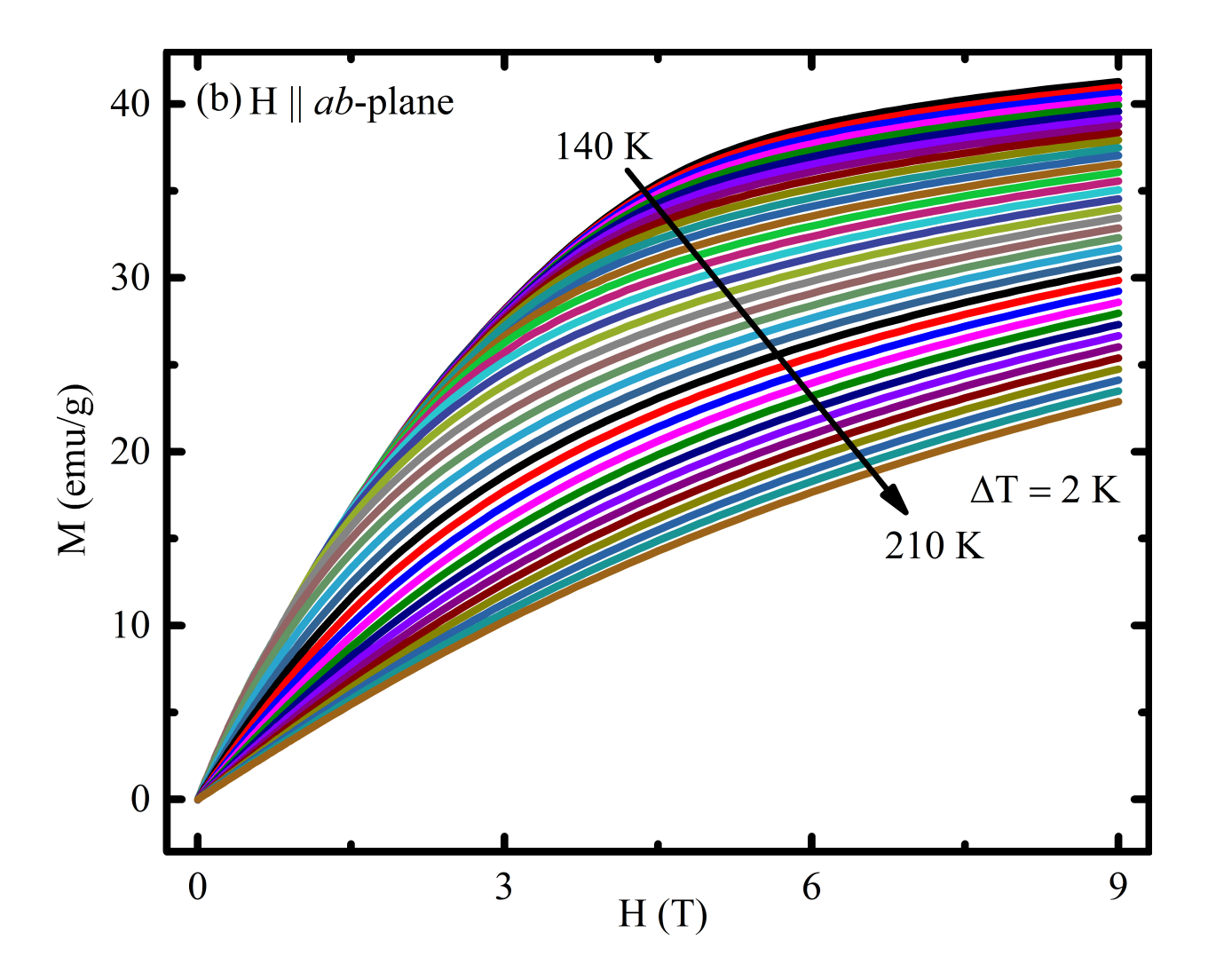


Figure 5: Isothermal field-dependent magnetizations along the (a) *c*-axis and (b) *ab*-plane around the paramagnetic to ferromagnetic transition from 140 K to 210 K.

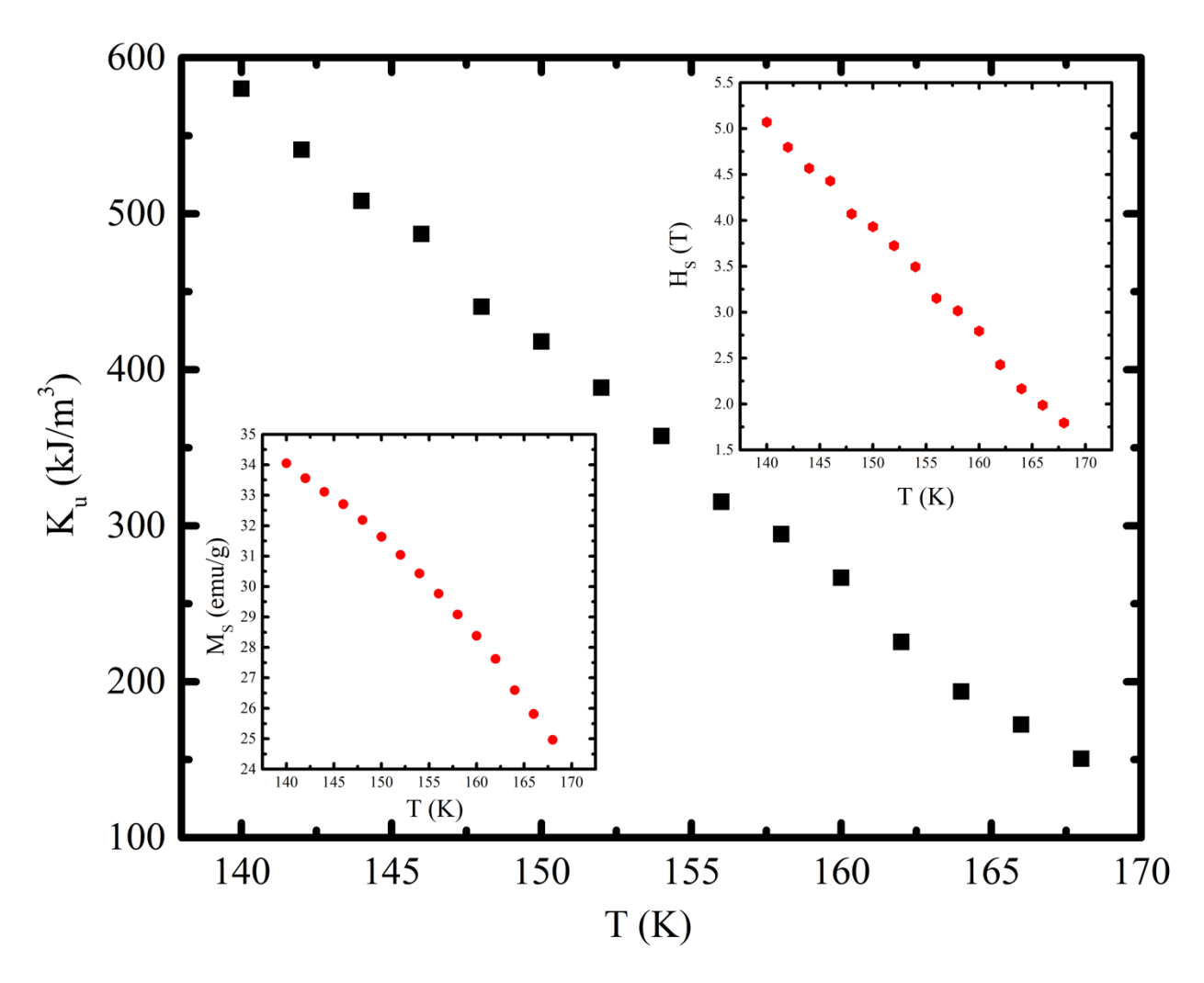
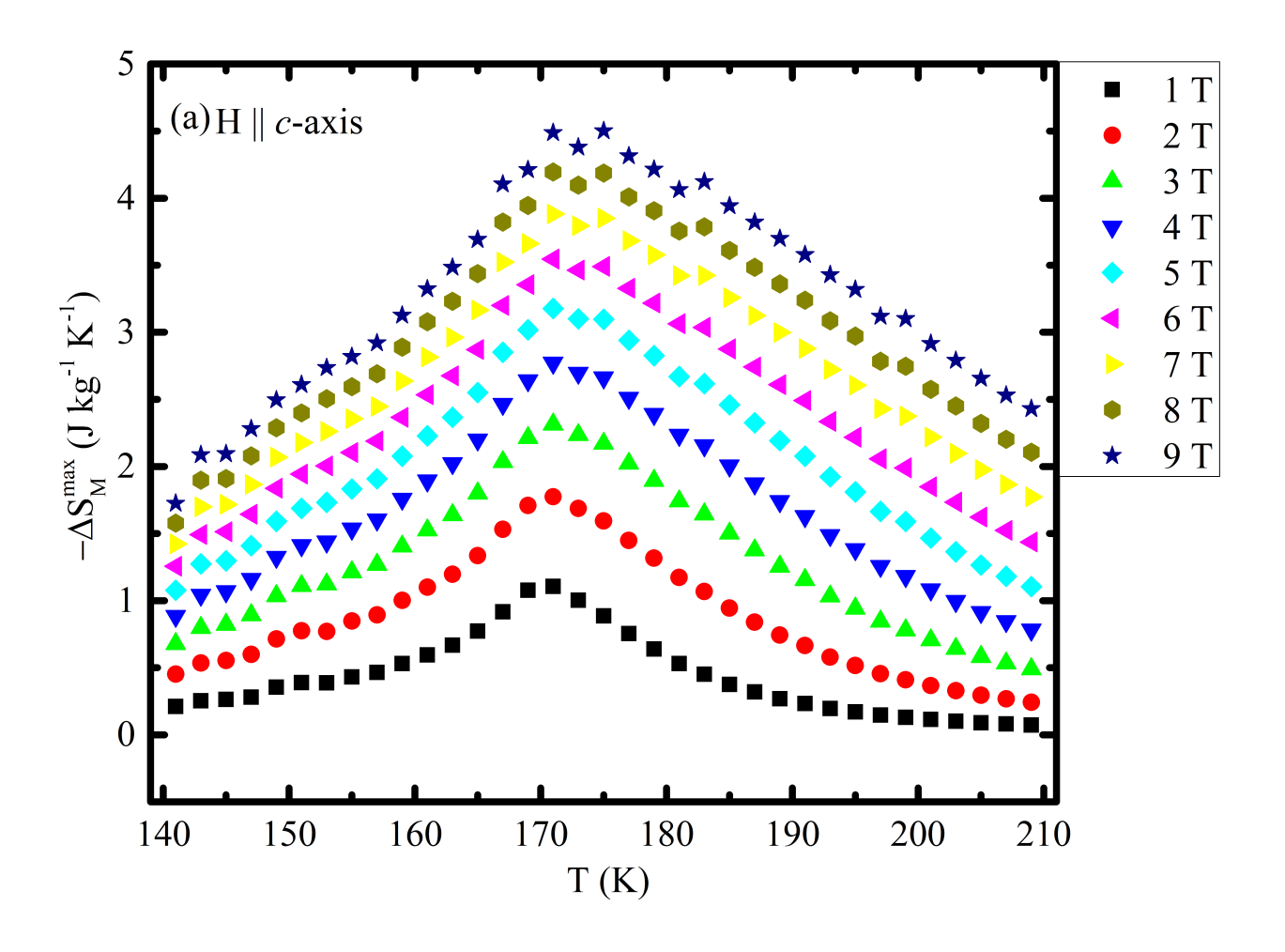
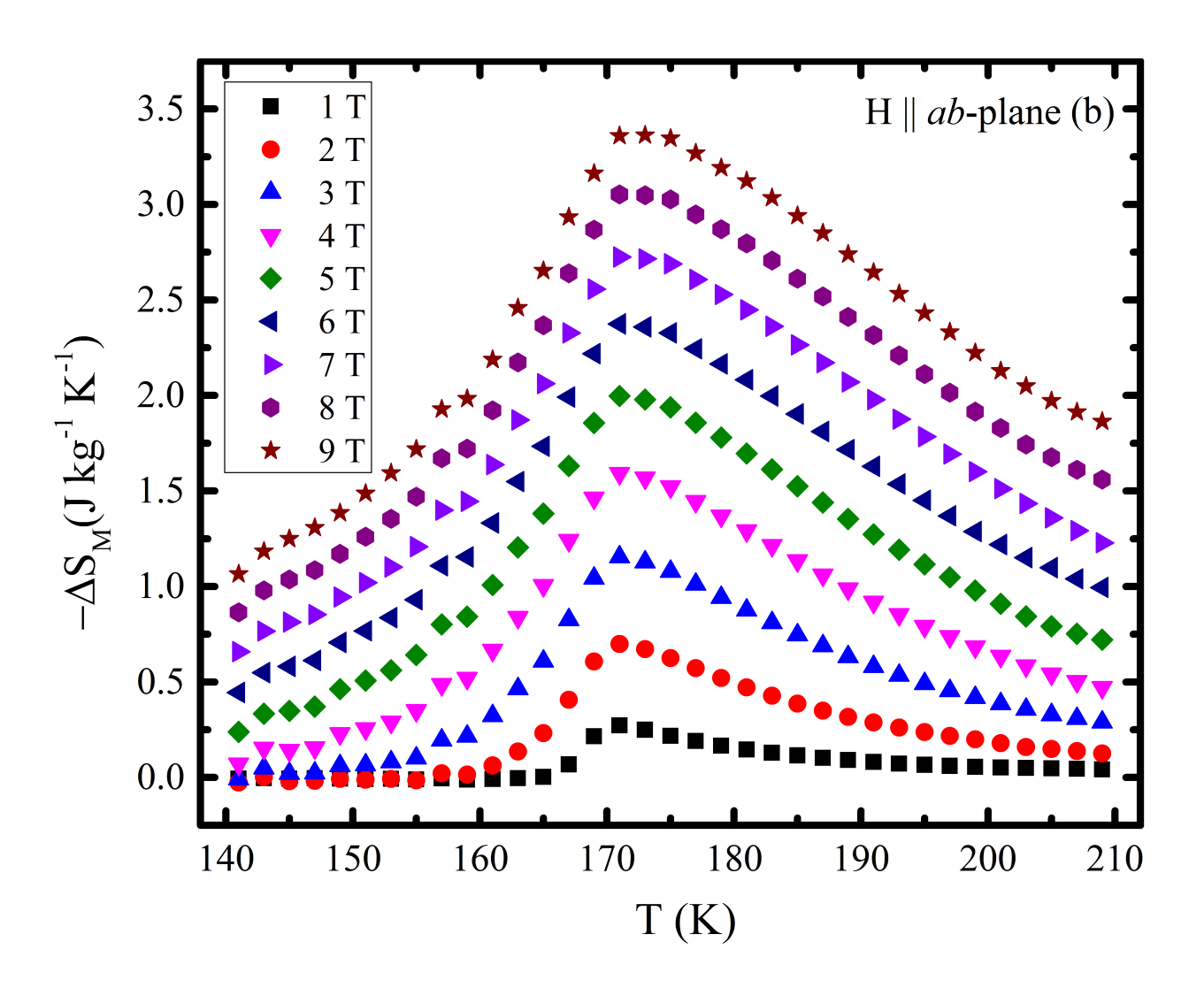


Figure 6: Temperature dependence of the calculated anisotropy constant  $K_u$ , the estimated saturation field  $H_S$  (inset), and the saturation magnetization  $M_S$  (inset) below transition temperature.





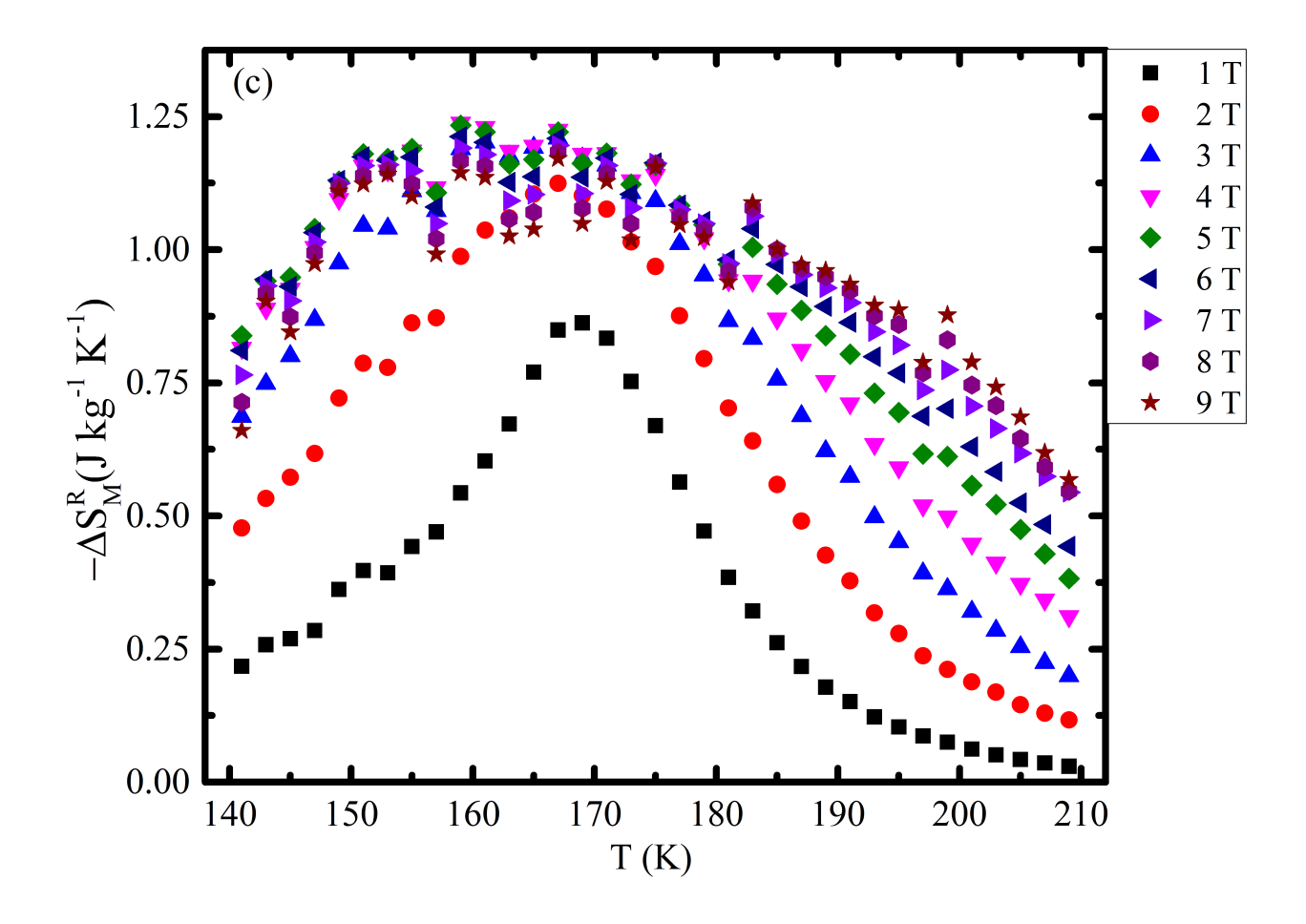
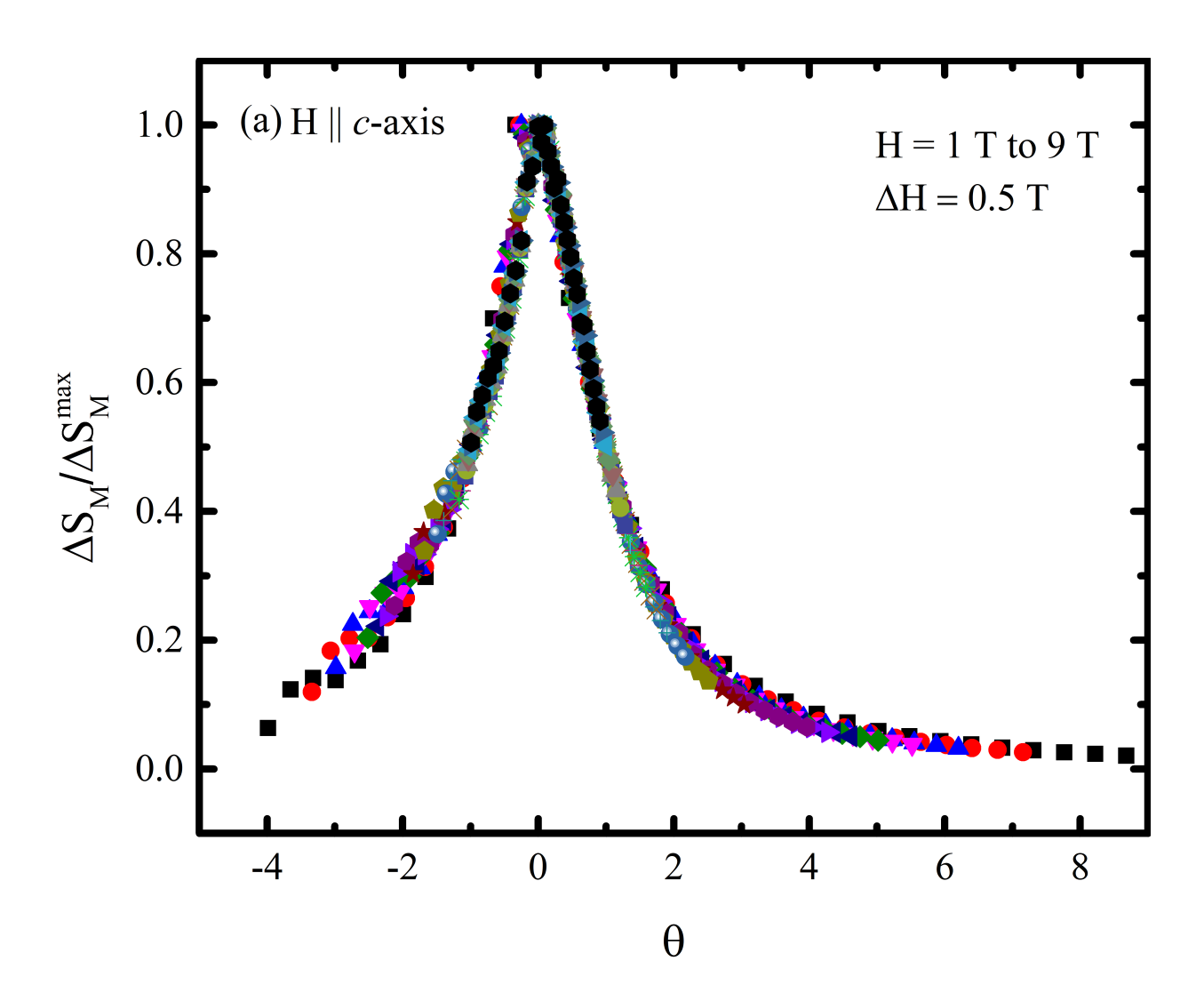


Figure 7: Temperature dependence change of magnetic entropy change with increasing magnetic field along the (a) c-axis and (b) the ab-plane near the paramagnetic to ferromagnetic phase transition. (c) Temperature dependence of magnetic entropy change  $-\Delta S^R_M$  obtained by rotating from the ab-plane to the c-axis in various fields.



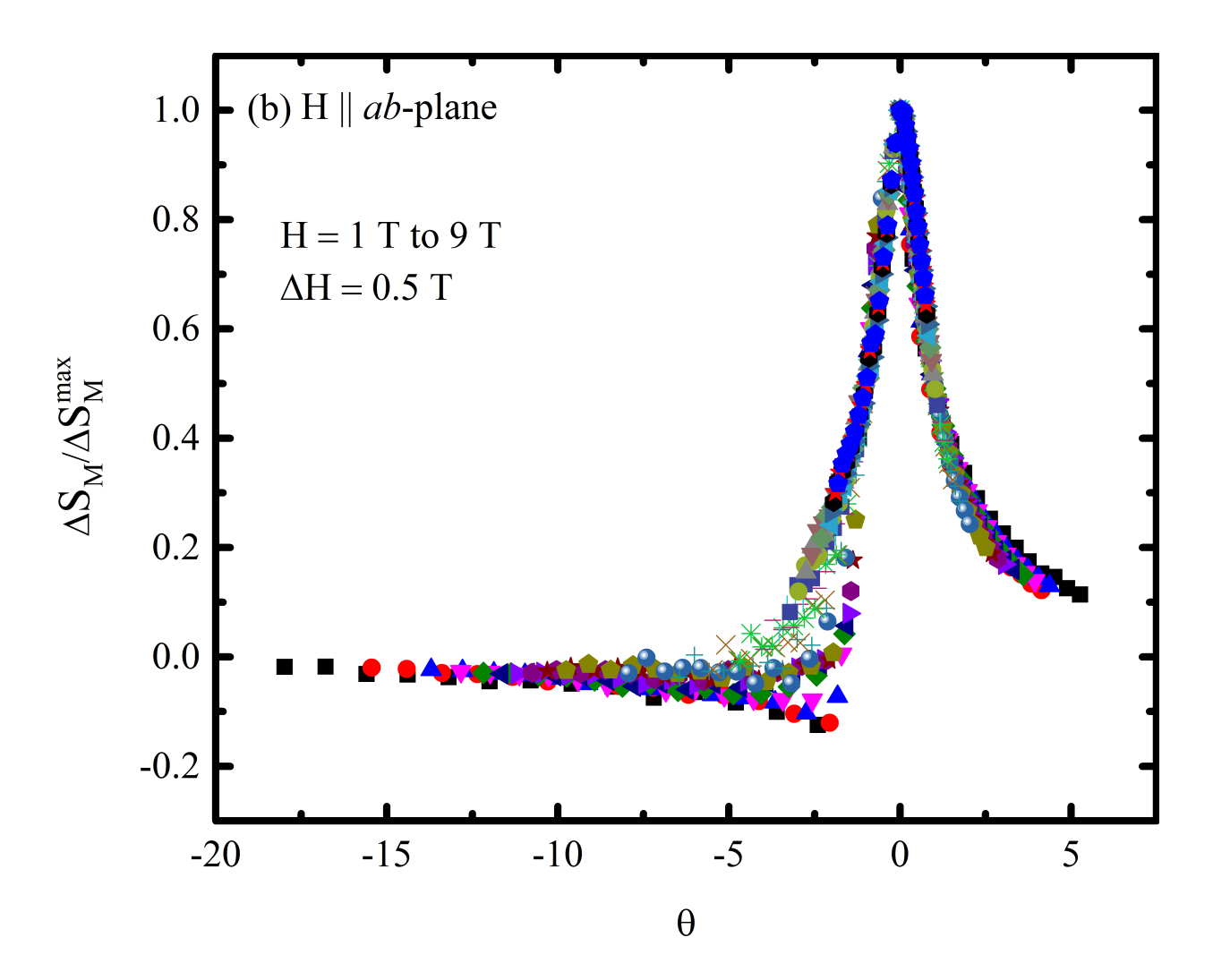
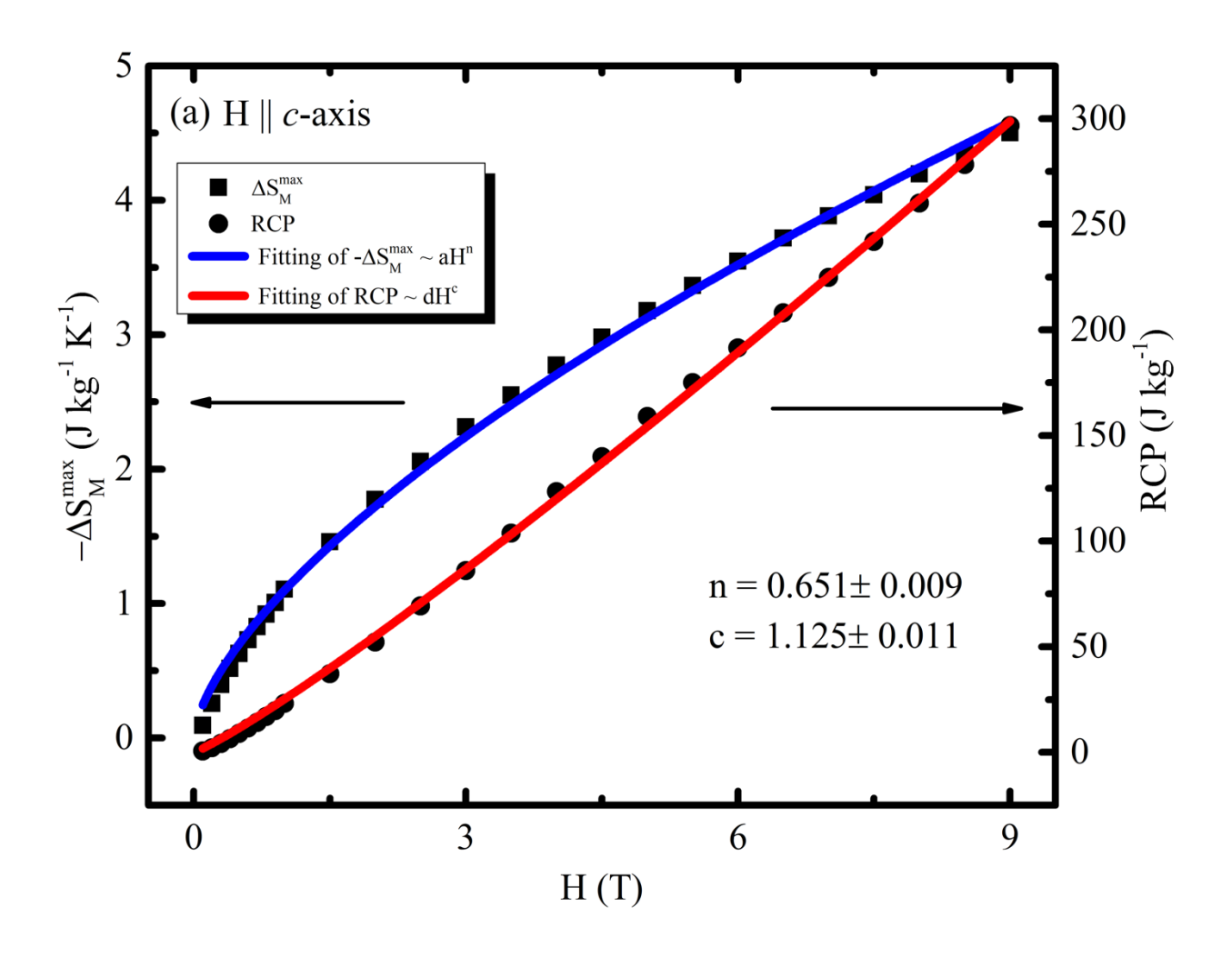


Figure 8: The normalized magnetic entropy ( $\Delta S_M/\Delta S_M^{max}$ ) as a function of rescaled temperature  $\theta$  along the (a) c-axis and (b) ab-plane.



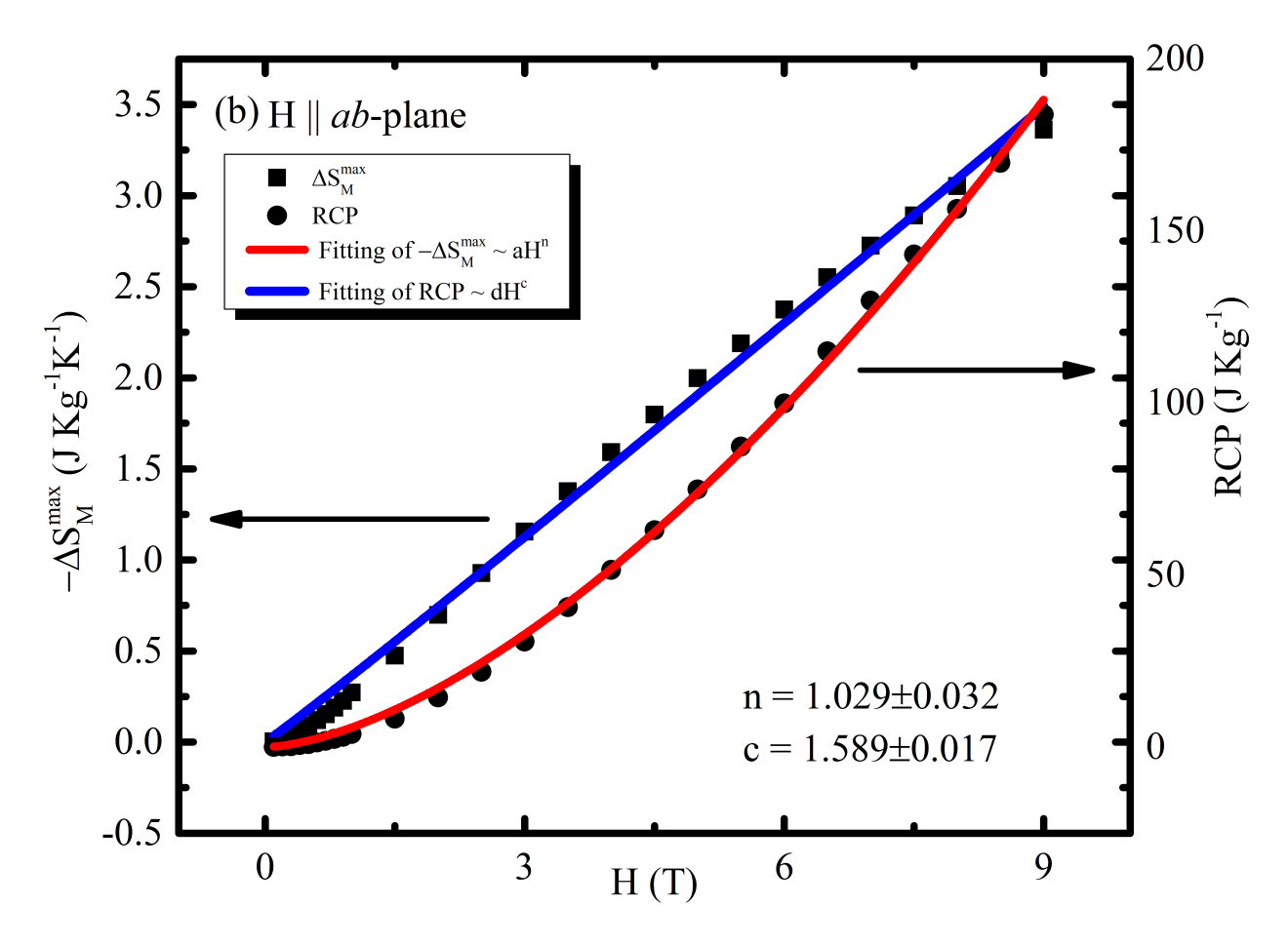
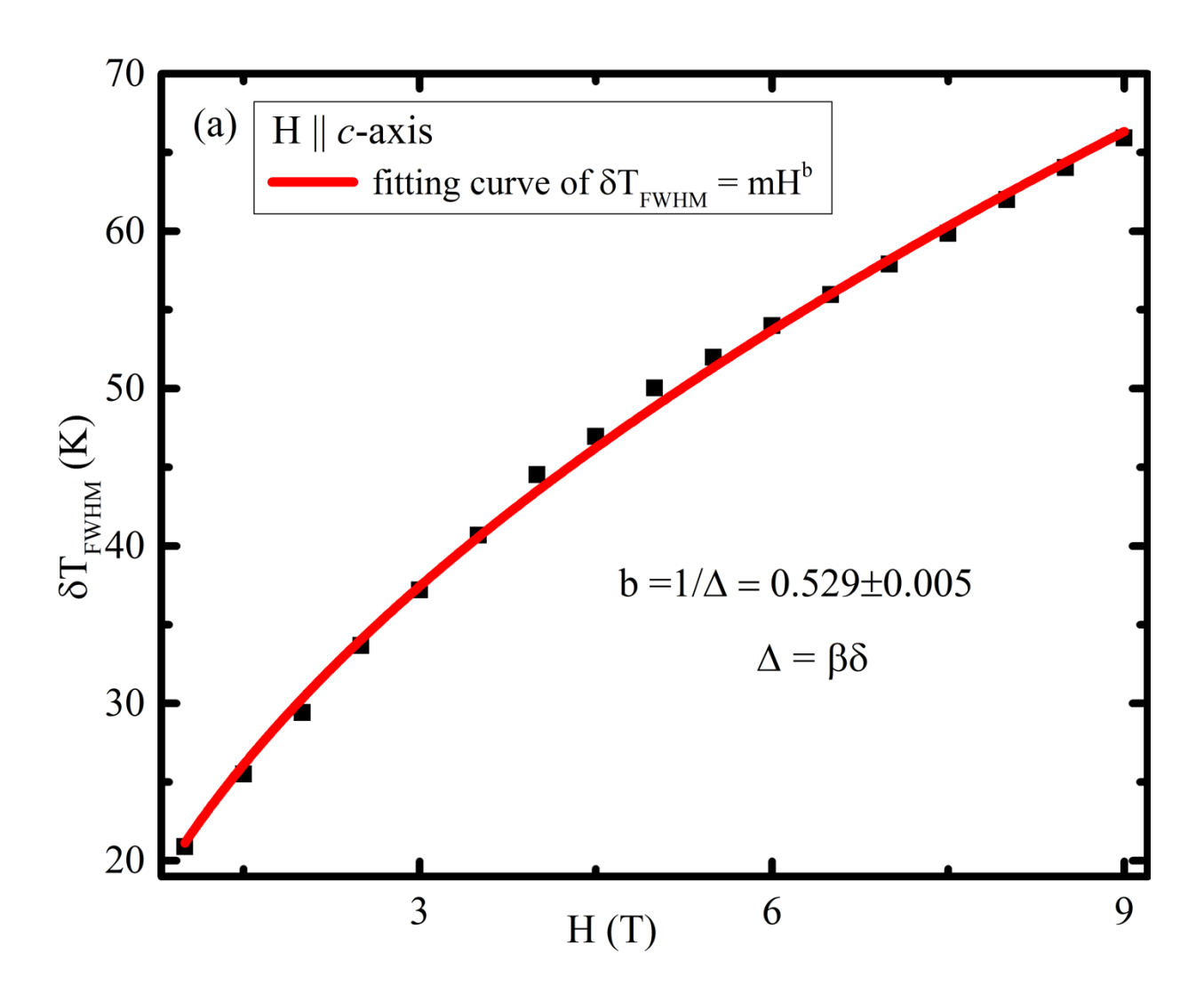


Figure 9: Magnetic field dependence of the maximum magnetic entropy change  $-\Delta S^{max}_{M}$  and the relative cooling power (RCP) with power-law fitting in blue and red solid lines, respectively for field applied along the (a) c-axis and (b) ab-plane.



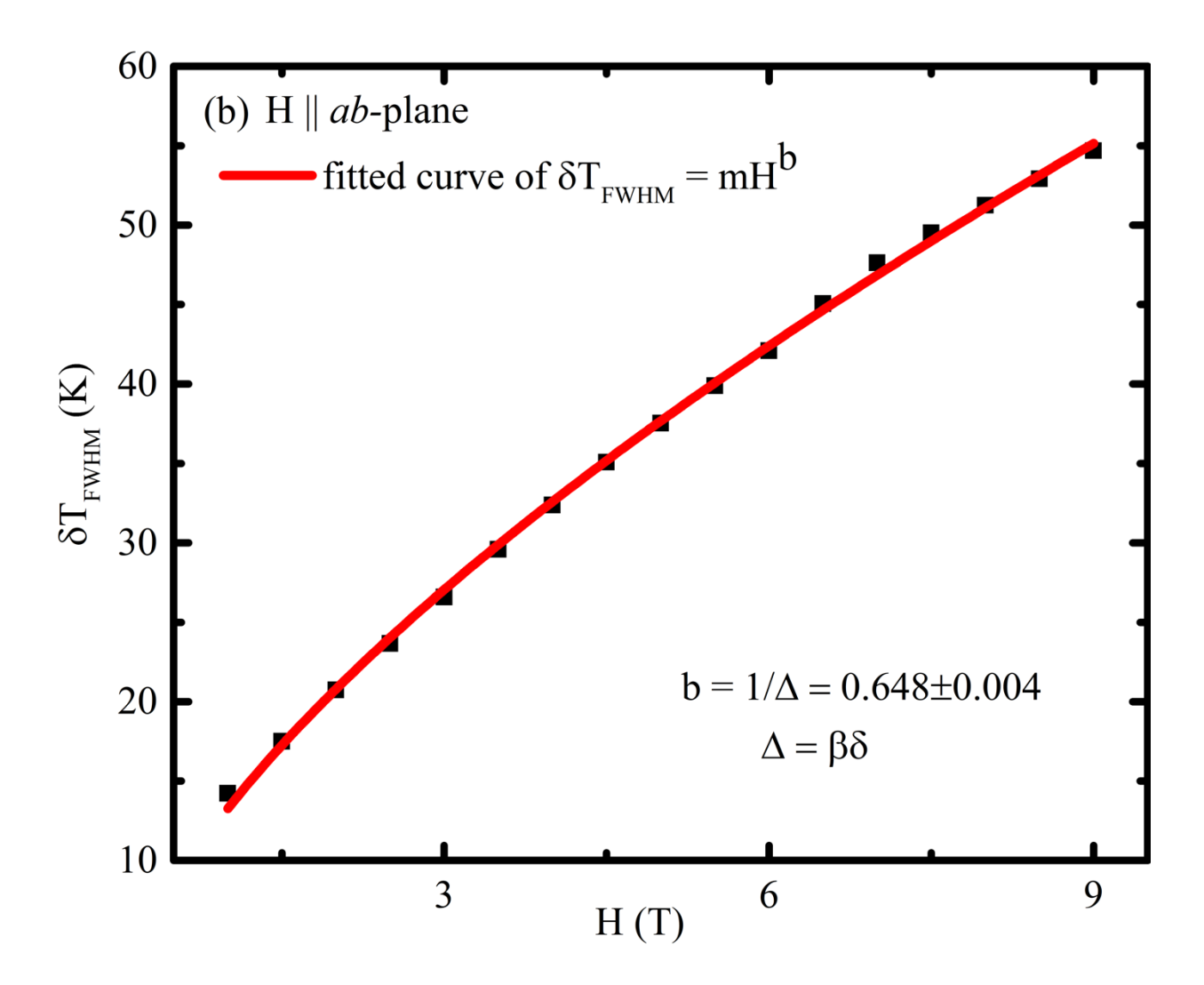


Figure 10: Magnetic field dependence of calculated  $\delta T_{FWHM}$  with fitting curve for magnetic field applied along the (a) *c*-axis and (b) *ab*-plane.

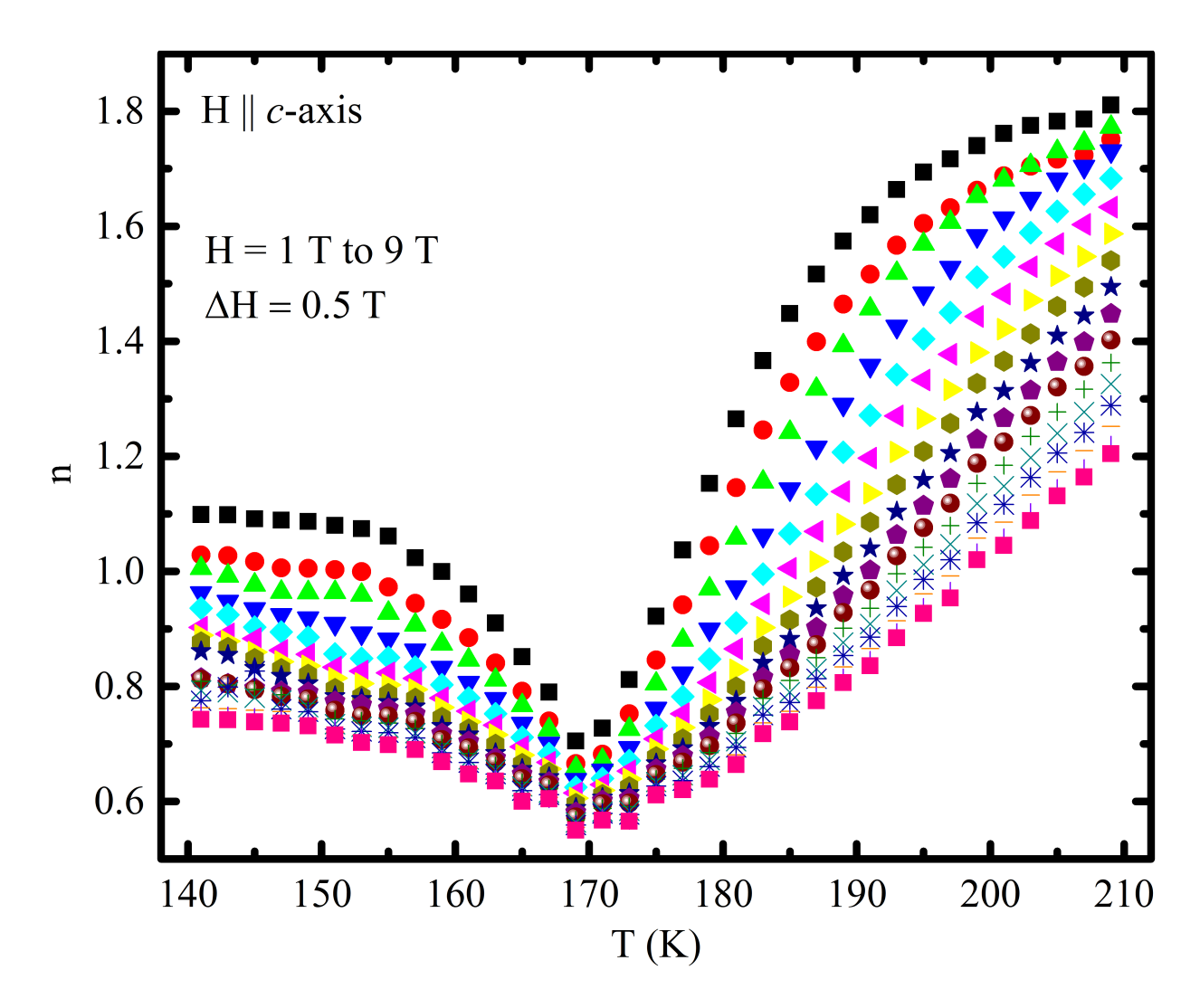
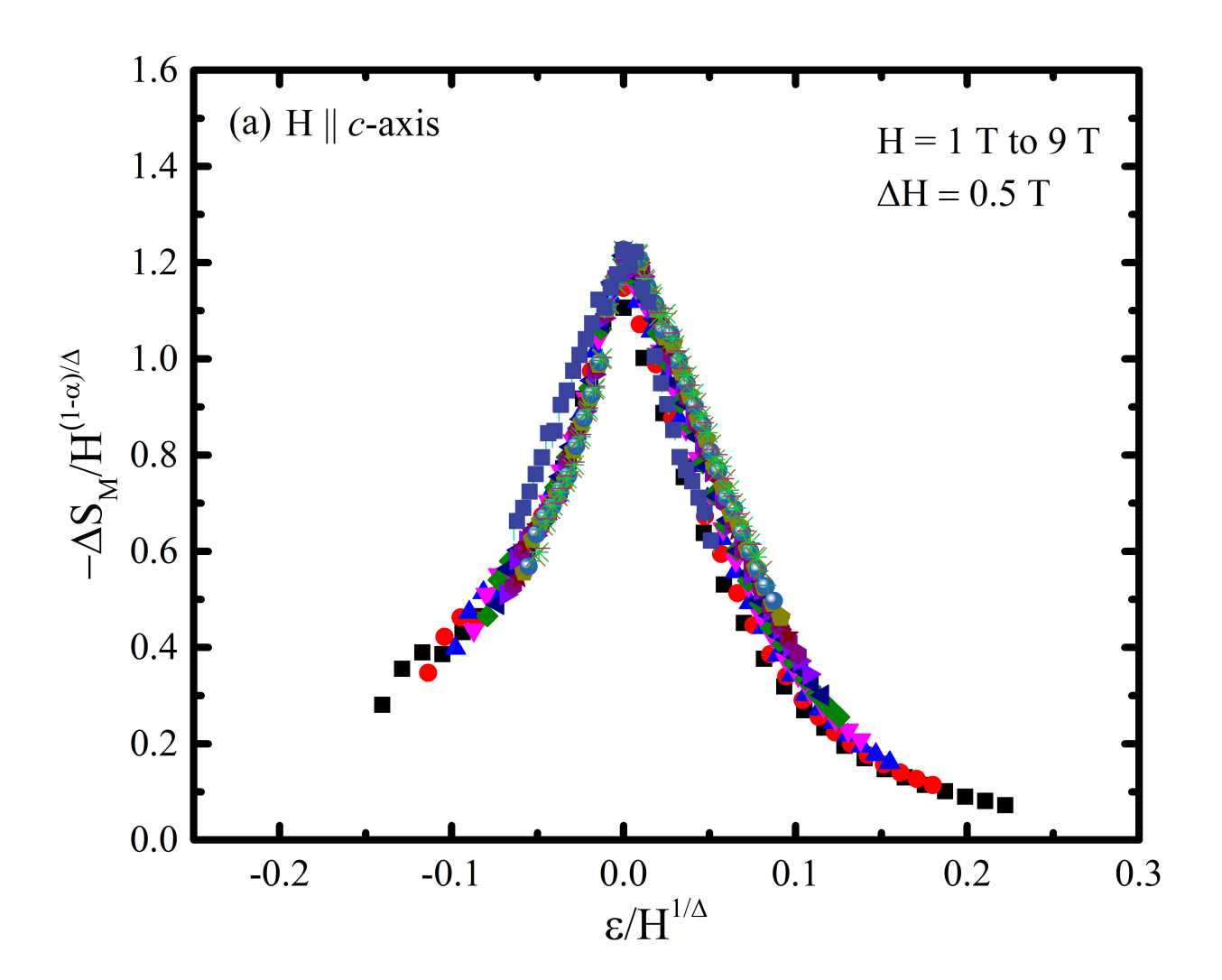


Fig 11: Temperature dependence of n for various magnetic fields applied along the c-axis.



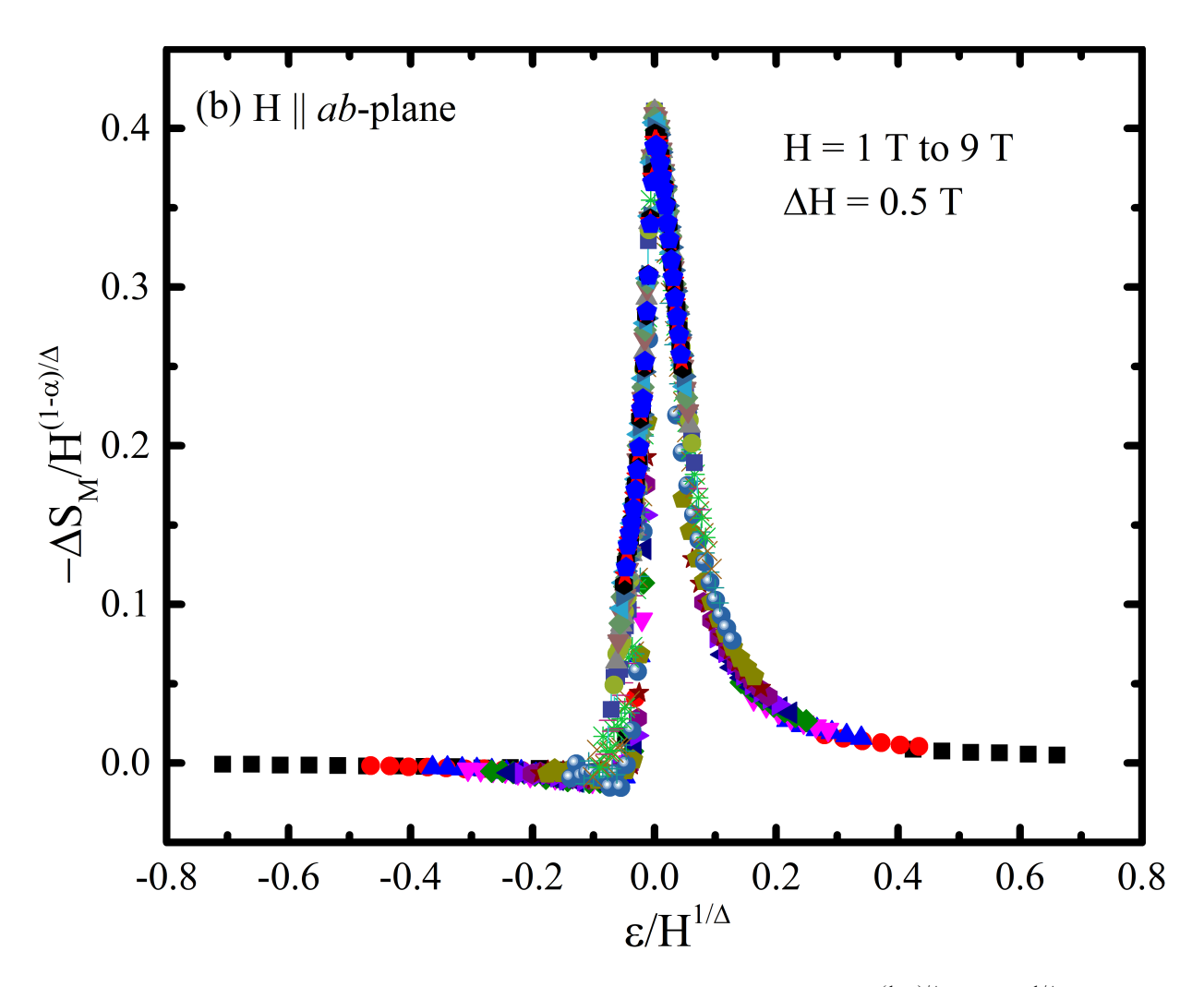
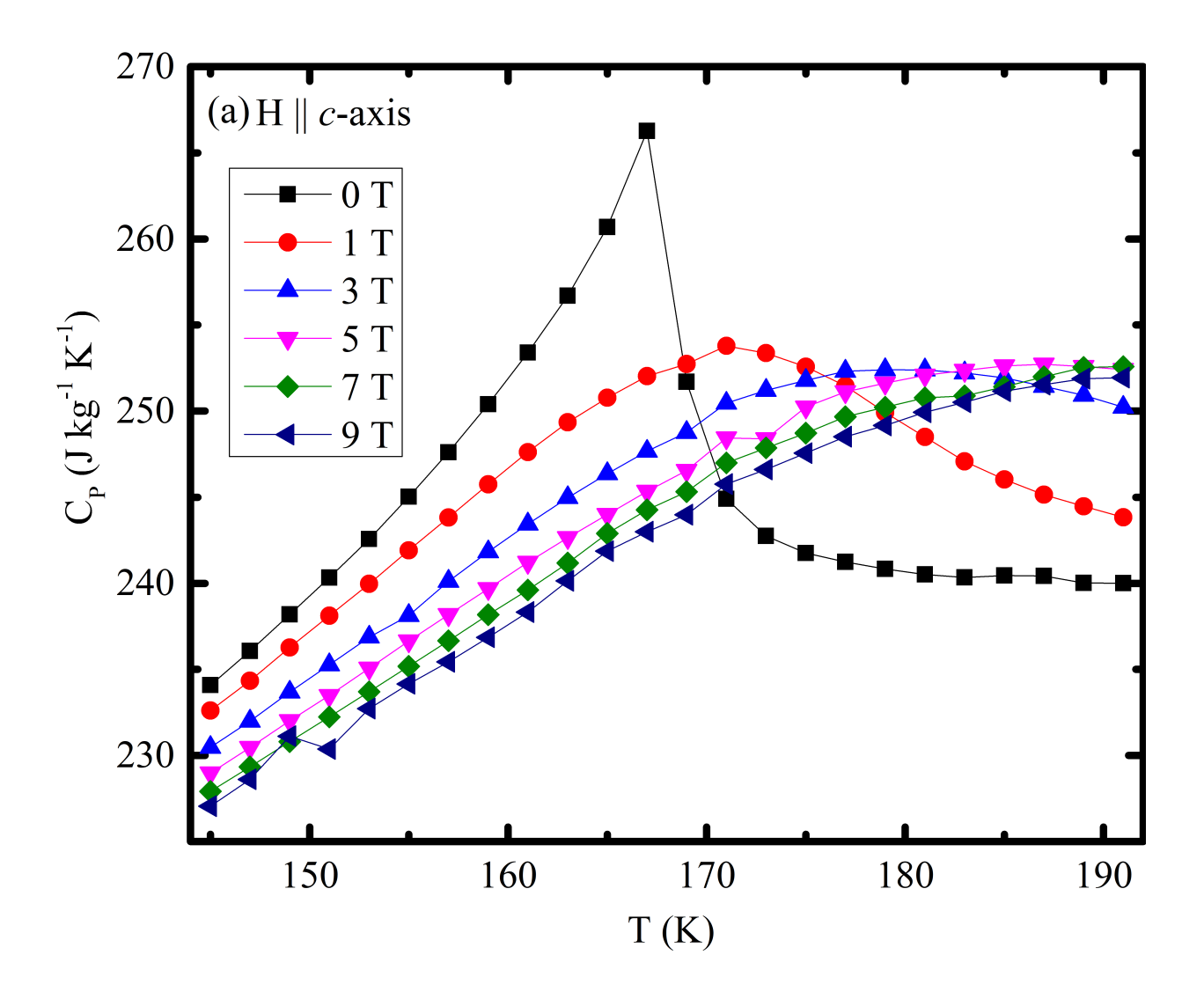
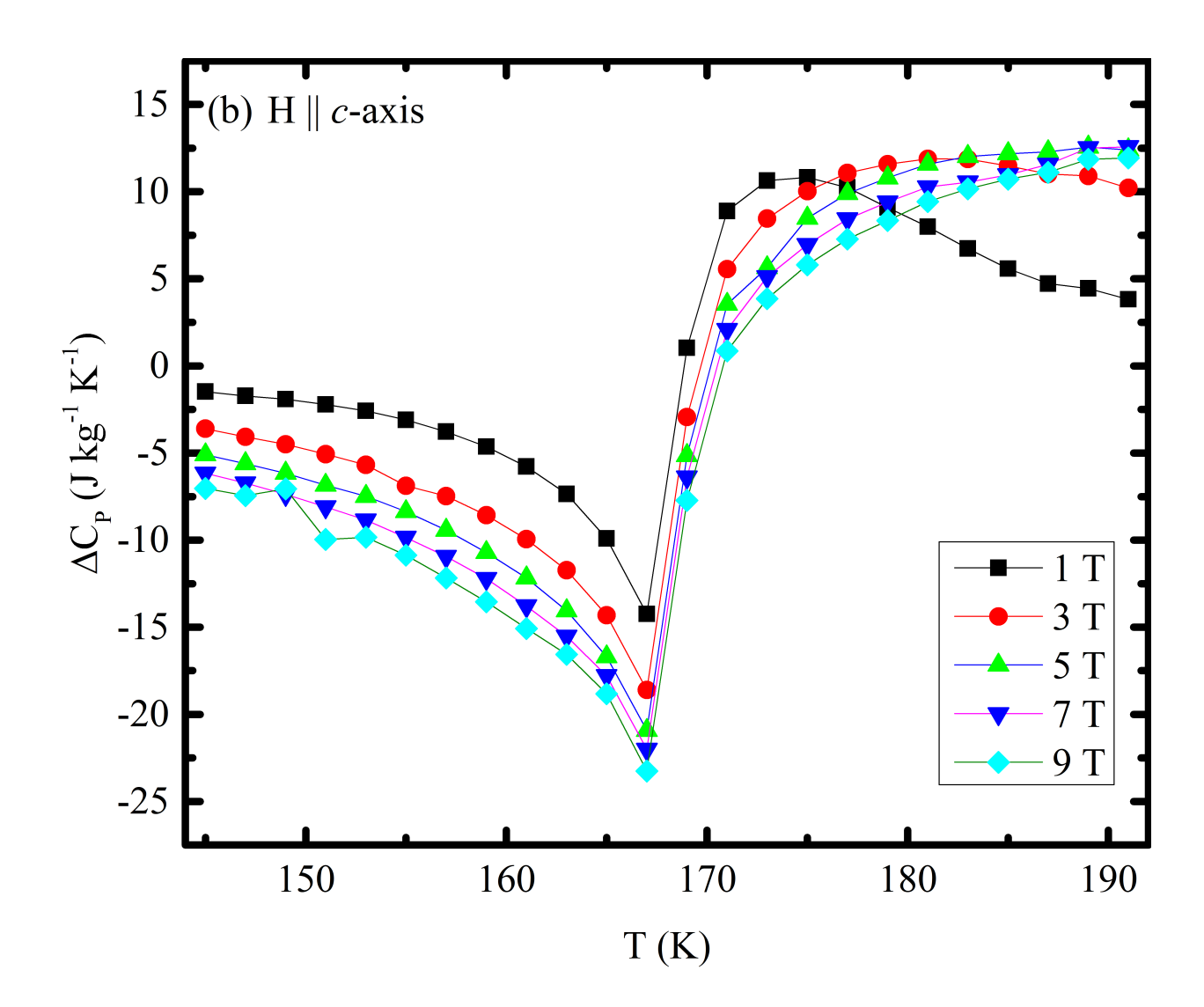
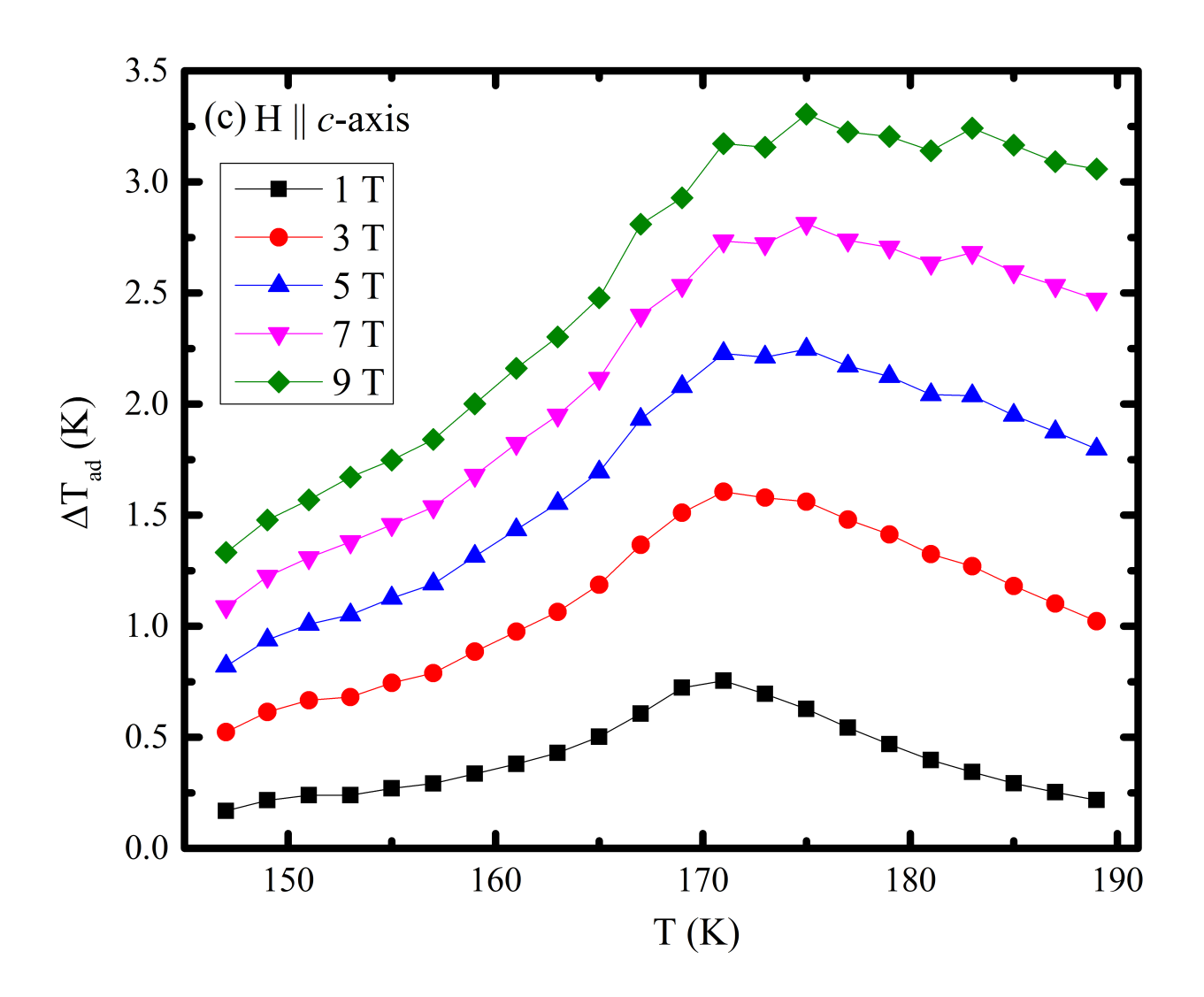


Figure 12: The scaling of change of magnetic entropy curves:  $-\Delta S_M / H^{(1-\alpha)/\Delta} vs. \epsilon / H^{1/\Delta}$  along the (a) *c*-axis and (b) *ab*-plane.







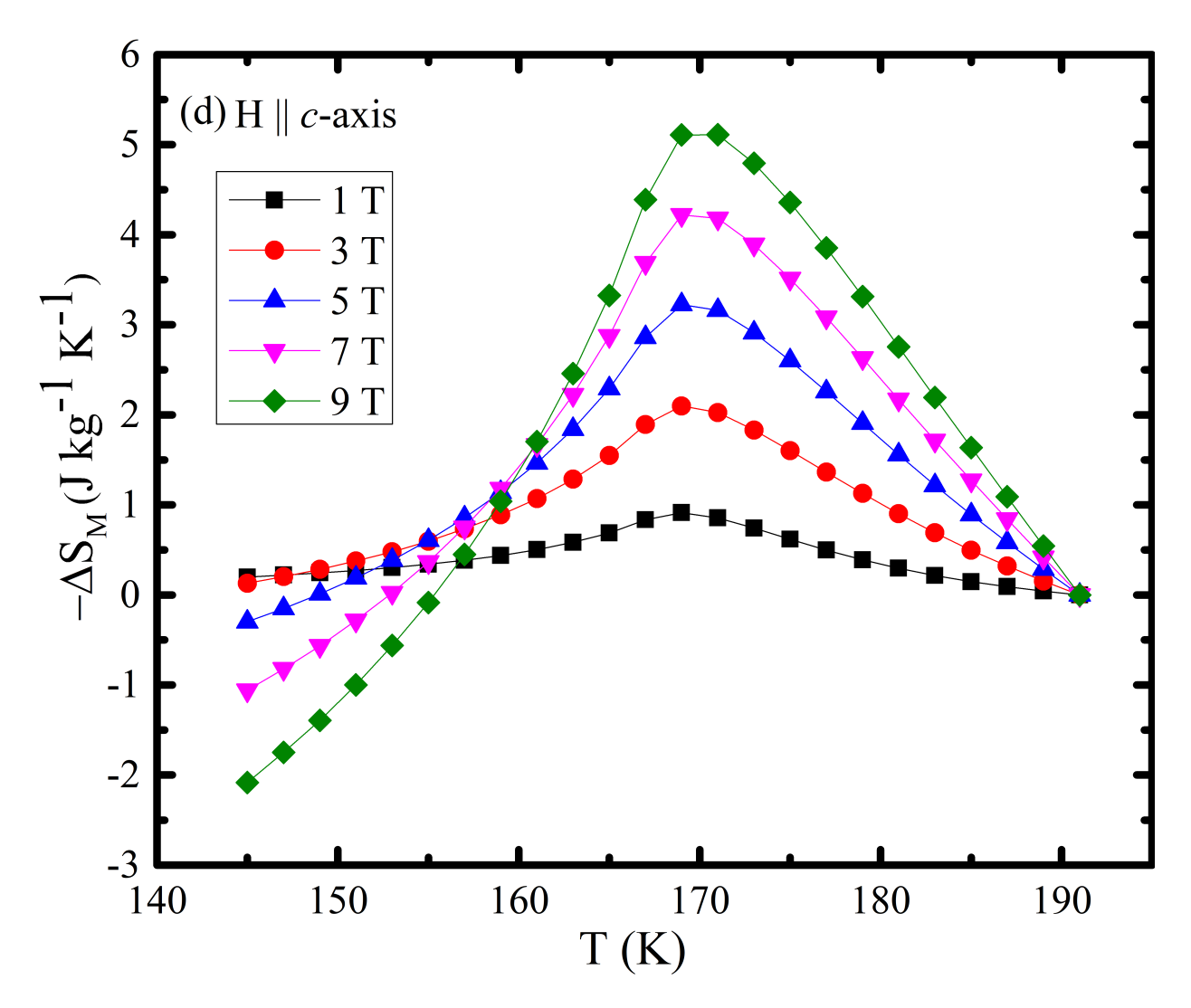


Figure 13: (a) Temperature dependence of single crystal  $Cr_2Te_3$  sample specific heat for different magnetic fields applied along the c-axis. (b) Temperature dependence of change of specific heat  $[\Delta C_p = C_p(T, H) - C_p(T, 0)]$  for different magnetic fields applied along the c-axis. (c) Temperature dependence of adiabatic temperature change  $\Delta T_{ad}$  for single crystal  $Cr_2Te_3$  sample estimated from heat capacity data for different magnetic fields. (d) Temperature dependence change of magnetic entropy estimated from heat capacity for different magnetic fields applied along the c-axis.

## For Table of Contents Use Only

